Original Article

Finite Element-Integrated Deep Learning Model for Early Risk Detection of Work-Related Musculoskeletal Disorders

Abdulmajeed Azyabi[1]

[1]Department of Industrial Engineering, College of Engineering and Computer Sciences, Jazan University, Jazan, Saudi Arabia, P.O. Box 706, Jazan 45142.

Abstract : Work-related musculoskeletal disorders (WMSDs) are an important occupational-health concern in textile and other manufacturing settings because many tasks involve repetitive upper-limb motion. Conventional machine-learning WMSD prediction models and ergonomic assessments generally rely on historical posture data and rarely combine biomechanical constraints with ahead-of-time (AoT) forecasting. This study proposes the Finite Element with Puma Optimized Deep Network for Proactive WMSD Prediction (FEPO-WMSDNet). The framework uses a Finite Element–Integrated Neural Network (FEINN) for biomechanical motion forecasting, a Puma Optimizer (PO) for adaptive hyperparameter tuning, and a Convolutional Karcı Fractional Artificial Neural Network (CK-FANN) for binary risk classification using study-derived rules based on RULA and ISO 11226. The framework was evaluated through a secondary analysis of the publicly available UI-PRMD dataset, using Vicon joint-angle recordings from 10 healthy subjects; no industrial workers were recruited for the present study. Under the reported subject-level evaluation, with each metric averaged across the three shoulder-angle components, FEPO-WMSDNet attained a mean Matthews correlation coefficient of 0.955, accuracy of 96.5%, F1-score of 96.1%, precision of 95.2%, recall of 96.9%, and specificity of 98.2% for risk classification. For AoT motion-angle forecasting, it attained R^2 of 0.981, average MAPE of 3.60%, RMSE of 0.063°, and MAE of 0.043°. These results support the framework as a promising benchmark on UI-PRMD, while validation on occupational cohorts remains necessary before claims of workplace effectiveness can be made.

Keywords: WMSD risk prediction, human-motion forecasting, finite element neural network, fractional-order learning, UI-PRMD dataset.

Address for correspondence:
E-mail: aazyabi@jazanu.edu.sa
Received: 16-12-2025; **Revision: 16-8-2026**; **Accepted:** 16-10-2026;
Published: 22-10-2026

1 Introduction

Textile and garment production increasingly relies on continuous interaction between human operators and automated machinery [1]. Repetitive and physically demanding tasks expose workers to sustained muscle and joint loading [2], thereby increasing the risk of work-related musculoskeletal disorders (WMSDs). These disorders affect worker health and safety and may reduce productivity and product quality while contributing to absence and premature retirement [3, 4]. Early detection and prevention are therefore priorities in occupational health and industrial ergonomics [5].

Machine-learning methods are increasingly used in ergonomics, robotics, posture monitoring, health, and sports to analyze and predict human motion [6, 7]. Recent studies have combined optoelectronic or inertial motion-capture systems with machine-learning models to classify movement and posture patterns [8, 9]. However, most approaches focus on activity recognition or current-posture assessment; comparatively few have examined ahead-of-time forecasting of potentially hazardous motion associated with WMSDs [10].

Despite these advances, important limitations remain [11]. Many models rely only on past or current motion and therefore provide limited warning before a harmful posture occurs [12, 13]. In addition, tightly coupled architectures can be difficult to update when the forecasting model, optimization strategy, or ergonomic decision rule changes, which constrains scalability and reuse [14, 15].

To address these limitations, this study proposes a deep-

learning framework that combines human-motion forecasting with ergonomics-based risk evaluation. Upper-limb kinematic data were obtained from the public UI-PRMD motion-capture dataset and processed as subject-specific time series. A forecasting network predicts future shoulder-angle trajectories, and the predicted trajectories are evaluated using predefined ergonomic rules to classify upcoming windows as normal or risk. The framework is intended as a basis for future preventive applications, such as alarms or adaptive assistance; however, the present work is an offline secondary analysis and does not constitute an industrial deployment. The main contributions are as follows:

- FEPO-WMSDNet integrates finite element modeling with a deep neural network through FEINN to encourage biomechanically consistent motion forecasts.
- The Puma Optimizer tunes selected FEINN hyperparameters with the objective of reducing validation error and improving convergence stability.
- The framework performs ahead-of-time forecasting of shoulder-angle trajectories so that study-derived risk conditions can be identified before the forecast horizon is reached.
- CK-FANN combines convolutional feature extraction with fractional-order learning to classify each forecast window as normal or risk.

The paper is organized as follows: Section 2 reviews related works; Section 3 presents the proposed FEPO-WMSDNet methodology; Section 4 discusses results and performance evaluation; and Section 5 concludes with findings and future work.

2 Literature Survey

Antwi-Afari et al. [16] combined wearable insole-pressure measurements with LSTM, BiLSTM, and GRU models to recognize awkward construction postures. The GRU achieved 99.01% accuracy, with F1-scores ranging from 93.19% to 99.39%. Although the approach captures sequential patterns effectively, its performance depends on sensor quality and entails non-trivial computational cost. Jiao et al. [17] developed an automated REBA assessment method based on three-dimensional pose reconstruction from workplace video. The method achieved an average precision of 94.7%, comparable with expert evaluation, but depends on high-quality video and substantial computational resources.

Ciccarelli et al. [18] proposed SPECTRE, a sensor-independent parallel deep-convolutional network for workplace-posture classification and segment-level ergonomic assessment. Its evaluation included metrics appropriate for imbalanced data, such as precision, recall, F1-score, and area under the precision-recall curve. The architecture improves interpretability but remains computationally complex.

Sheik Abdullah et al. [19] used transfer-learning CNNs to recognize five recurrent seated postures among adults working from home. Xception produced the strongest results and supported real-time monitoring, although performance remained sensitive to camera quality and ambient lighting.

Huang et al. [20] introduced a spatial-relationship-aware fuzzy whole-body assessment based on deep-learning three-dimensional pose reconstruction and smoothed transitions between REBA risk levels. The method reported 99.31% precision on vehicle-production-line data, but its reconstruction pipeline increases computational requirements.

Ogundokun et al. [21] developed a posture-classification framework combining InceptionV3 with an SVM, LASSO-based feature selection, data augmentation, dropout, and early stopping. The model achieved 95.42% accuracy and an AUC of 99.35%, but its multi-stage architecture has relatively high computational cost.

Su et al. [22] proposed a decision-tree scheme for identifying WMSD risk patterns among sewing-machine operators. Body angles extracted from workplace video were evaluated with REBA-based rules and a C4.5 decision tree, producing 95% prediction accuracy and 83% path coverage. The approach is interpretable but depends on reliable video-based angle estimation.

Matos et al. [23] combined motion capture, time-series forecasting, ergonomic risk assessment, and an alarm mechanism for proactive WMSD prevention in manufacturing. Shoulder motion from 12 textile-machine operators was evaluated with 12-fold cross-validation, with SVM providing the strongest AoT forecasting and risk-detection performance among the tested methods. Nevertheless, the limited participant cohort constrains external generalization. Yildiz and Das [24] developed a flex-sensor and ANN-based posture-correction system using data from 12 participants across three sessions. The system reduced the predicted poor-posture count by 56.27%, but the small participant group and short observation period limited the strength of the

conclusions.

Jung et al. [25] evaluated logistic regression, SVM, decision tree, random forest, and XGBoost models for assessing the work-relatedness of shoulder musculoskeletal disorders in 7,270 compensation cases. Random forest achieved 84.46% accuracy, whereas XGBoost achieved 81.64% accuracy and an AUC of 0.73. The large administrative dataset improved consistency, although it represented a single national compensation system.

Table 1. Summary of recent posture-recognition and WMSD-risk studies

Author	Method	Result	Advantage	Disadvantage
Antwi-Afari, M.F. et al. [16]	RNN models (LSTM, Bi-LSTM, GRU) for posture recognition	GRU model achieved 99.01% accuracy and F1-score between 93.19%–99.39%	High accuracy and effective sequential pattern learning	High computational complexity and dependence on sensor data quality
Jiao, Z. et al. [17]	REBA using 3D pose reconstruction	Achieved 94.7% precision comparable to expert evaluation	High accuracy, automation, and generalization across industries	Reliance on high-quality video input and computational resources
Ciccarelli, M. et al. [18]	SPECTRE for posture classification	Demonstrated good performance using imbalanced data metrics (precision, recall, F1, AUPRC)	Sensor independence and explainability	Complex architecture and high computational requirements
Sheik Abdullah, A. et al. [19]	CNN for classifying sitting postures	Xception model achieved best classification accuracy	Real-time monitoring and improved ergonomic awareness	Dependent on camera quality and lighting conditions
Huang, K. et al. [20]	Spatial relationship-aware fuzzy REBA	Achieved 99.31% precision on automobile production line data	High accuracy and dynamic risk evaluation	High computational complexity and dependency on 3D data quality
Ogundokun, R.O. et al. [21]	InceptionV3-DCNN hybridized with SVM and LASSO	Achieved 95.42% accuracy and 99.35% AUC	High robustness and accuracy; effective overfitting prevention	High computational cost and model complexity
Su, J.M. et al. [22]	DTAS-EAWP	Achieved over 95% prediction accuracy and 83% path coverage	High interpretability and automation for risk prediction	Dependent on video quality and limited generalization
Matos, L.M., et al. [23]	Proactive WMSD Prevention Method using MCS, TSF with ML, and ergonomic risk assessment	SVM achieved best Ahead-of-Time forecasting and WMSD detection accuracy	Accurate early detection and moderate computational cost	Limited participant diversity
Yildiz, E. and Das, M., [24]	Flex sensor–based posture correction and prediction system using Artificial Neural Network (ANN)	Poor Posture Count (PPC) reduced by 56.27%, showing improved posture learning habits	Effective posture improvement and reliable PPC prediction	Small sample size and short experimental duration
Jung, S., et al. [25]	Machine learning models (Logistic Regression, SVM, Decision Tree, Random Forest, XGBoost) for work-relatedness prediction	Random Forest achieved 84.46% accuracy, XGBoost 81.64% (AUC 0.73)	Improved decision consistency and reliable prediction of work-relatedness	Dataset limited to a single national database

Table 1 shows that recent posture-recognition and ergonomic-risk studies achieve strong classification performance using RNNs, CNNs, pose reconstruction, and decision trees. However, most evaluate recognition or current-risk assessment rather than AoT forecasting, and their reported performance is often coupled to specific sensors, video conditions, or narrowly defined populations.

2.1 Recent Deep Learning Approaches for Motion Forecasting and Ergonomic Risk Prediction

Recent deep learning research on motion forecasting clusters into four architectural families: attention-based sequence models, temporal convolutional networks, physics-informed networks, and graph-based motion models. None was developed for occupational ergonomics. This section therefore assesses each against the six criteria that matter for proactive WMSD prediction, namely physical consistency, temporal modeling capacity,

generalization to unseen participants, data requirements, computational cost, and ergonomic interpretability, instead of summarizing the studies one by one.

Attention-based sequence forecasters. The Temporal Fusion Transformer [29], Informer [30], Autoformer [31], and PatchTST [32] all target long-horizon multivariate forecasting, and their contributions are largely complementary. TFT adds variable selection and interpretable attention heads. Informer replaces full self-attention with a sparse variant to escape its quadratic cost. Autoformer substitutes series decomposition and auto-correlation for point-wise attention, while PatchTST tokenizes the input as subsequence patches. On temporal modeling this family has no equal among the four, since self-attention places no architectural ceiling on dependency range and can link distant time steps directly. The difficulties lie elsewhere. Nothing in these models constrains an output to a physically realizable joint configuration, so a forecast may be smooth, plausible in time, and anatomically impossible. Their published validation is also remote from the present setting: electricity load, traffic flow, weather, and financial series, none of which is human kinematic data and none of which resembles a ten-subject upper-limb recording. Data appetite compounds this. With no architectural prior the mapping must be learned from examples alone, which is precisely what a study with few independent subjects cannot supply, however many time samples those subjects generate.

Temporal convolutional networks. TCNs [33] rely on dilated causal convolutions. The practical benefits are real: gradients remain stable, training parallelizes easily, and memory demands sit below those of recurrent or attention-based alternatives, which makes the family attractive for deployment on an industrial floor. The cost is a bounded receptive field. Dependencies longer than the depth and dilation schedule permit simply cannot be represented, and extending that horizon means a deeper network. TCNs also carry no biomechanical prior, and Bai et al. [33] evaluated them on generic sequence-modeling benchmarks rather than on occupational motion.

Physics-informed neural networks. PINNs [34], with their later extensions and surveys [36, 37], take a different route. Governing equations enter the training objective as residual penalties, so predictions are pushed towards satisfying known physical laws instead of merely fitting observations. This is the only family here with an explicit mechanism for physical consistency, and its data efficiency follows directly from that mechanism, since a physical prior narrows the hypothesis space and lightens the reliance on large training sets. What PINNs cost is computation and patience. Residual constraints require higher-order automatic differentiation, training times lengthen, and balancing the data and physics loss terms is a well-documented source of optimization difficulty [37]. A further mismatch matters here: conventional PINNs presuppose a governing partial differential equation, and upper-limb ergonomic risk does not present itself in that form.

Graph-based motion models. Representing the skeleton as a graph, with joints as nodes and anatomical links as edges, preserves structural dependencies that a flat vector discards. Mao et al. [35] applied this idea to human motion prediction; Zachariah and Charitha [38] have since applied a graph autoencoder to ergonomic risk classification, which makes this the family whose published application sits closest to the present problem. Physical consistency here is partial. Skeletal connectivity is respected, but joint kinematics and tissue loading are not modeled explicitly. Generalization across subjects is reasonable because the topology is shared, though performance depends heavily on how the graph is constructed, and robust results normally demand more annotated data than ten subjects provide.

Evaluation context. One qualification applies across all four families and should be stated plainly. Apart from [38], none of the works cited above was evaluated on a work-related musculoskeletal disorder dataset, and none on a dataset of comparable participant count. Table 2 is therefore an assessment of documented architectural properties, not a transfer of reported benchmark figures, and should be read on those terms.

Criteria definitions. Ratings in **Table** 2 follow definitions fixed in advance. Physical consistency records whether biomechanical constraints enter architecturally (Explicit), follow implicitly from a structural representation (Partial), or are absent (None). Temporal modeling is rated High where architecture places no ceiling on dependency range and Moderate where a receptive field or recurrence depth bounds it. Participant-level generalization reflects expected robustness on unseen subjects, inferred from the strength of the architectural prior; data requirement, which varies inversely with that strength, reflects the training volume normally needed. Computational cost is relative to the other

families listed. Ergonomic interpretability records whether a model's internal quantities correspond to variables used in standardized ergonomic assessment such as RULA and ISO 11226.

Table 2. Architectural comparison of recent deep-learning approaches for proactive WMSD prediction. Ratings describe documented architectural properties rather than measured performance on UI-PRMD.

Model family	Physical consistency	Temporal modeling	Participant-level generalization	Data requirement	Computational cost	Ergonomic interpretability
TFT [29]	None	High	Moderate	High	High	Moderate
Informer [30]	None	High	Moderate	High	Moderate	Low
Autoformer [31]	None	High	Moderate	High	Moderate	Low
PatchTST [32]	None	High	Moderate	High	Moderate	Low
TCN [33]	None	Moderate (bounded receptive field)	Moderate	Moderate	Low	Low
PINN [34, 36, 37]	Explicit (PDE residual)	Moderate	Moderate-High	Low-Moderate	High	Moderate
GNN [35, 38]	Partial (skeletal topology)	Moderate	Moderate-High	High	Moderate	Moderate
FEPO-WMSDNet (proposed)	**Explicit (finite element)**	**High**	**Moderate-High**	**Moderate**	**Moderate**	**High**

Two limitations of this positioning should be acknowledged. The first is that none of the above constitutes empirical evidence of superiority on the present data. These are design justifications, and the comparison reported in Section 4 remains the proper basis for any performance claim. The second concerns uncertainty. The framework produces point forecasts and deterministic risk labels with no accompanying uncertainty estimate, and for a system meant to trigger preventive action that omission matters, since a forecast sitting near a RULA threshold warrants different handling from one far away from it. Neither the proposed method nor the baselines compared against it currently supply such a measure. Adding predictive uncertainty, whether through deep ensembles or a Bayesian last layer, is left to future work.

The same reasoning accounts for the alternatives not being adopted as the forecasting backbone. Attention-based forecasters offer the most flexible temporal modeling available, but flexibility is the least affordable property here; with ten subjects the real risk is a model that fits subject-specific movement idiosyncrasies instead of transferable postural dynamics, and nothing in those architectures discourages it. TCNs are computationally attractive but share the absence of a physical prior and add a bounded temporal horizon. Graph models are the nearest published analogue [38], yet they need a graph construction and an annotated volume this dataset cannot support.

2.2 Positioning of the Proposed FEINN Relative to Conventional Physics-Informed Learning

FEINN and conventional PINNs begin from the same premise: physical knowledge ought to constrain a learned model instead of being left for the network to infer. Where they part company is in how that knowledge is encoded, and for this application the difference is consequential.

A conventional PINN penalizes the residual of a governing differential equation at collocation points, which assumes the relevant physics is available in closed form. FEINN couples the network to a finite element discretization instead, so the prior arrives as nodal displacement, strain, and stress relationships taken from the element formulation. Three things follow. Physical consistency is enforced in quantities that map onto ergonomic assessment directly, namely segment displacement and tissue loading, which supports interpretation against RULA and ISO 11226 criteria instead of leaving it as an abstract residual. The finite element structure also supplies a strong inductive bias, reducing the training data needed for a given accuracy, and that is the binding constraint in a ten-subject study. Because the discretization is fixed by geometry and material parameters instead of being learned, its computational cost is incurred predictably, without the residual-balancing difficulties that characterize PINN training [37].

3 Methodology

The present work develops FEPO-WMSDNet, a deep-learning framework for forecasting upper-limb kinematics and classifying ergonomically risky motion windows. The workflow begins with the publicly available UI-PRMD dataset collected by Vakanski et al. [39].

UI-PRMD contains motion recordings from 10 healthy subjects performing physical-rehabilitation movements. The present analysis uses the Vicon joint-angle stream, originally sampled at 100 Hz, and extracts three left-shoulder angular components: abduction–adduction, internal–external rotation, and flexion–extension. The selected trajectories are low-pass filtered at the 100-Hz source rate, resampled to the 10-Hz working rate, normalized, and segmented only after subject-level fold assignment. FEINN performs AoT motion forecasting, while the Puma Optimizer tunes FEINN hyperparameters. CK-FANN then classifies the predicted windows as normal or risk using binary labels derived in this study from the RULA- and ISO 11226-based rules in **Table 3**. UI-PRMD itself does not provide WMSD diagnoses or these ergonomic risk labels. Figure 1 summarizes the resulting secondary-analysis workflow.

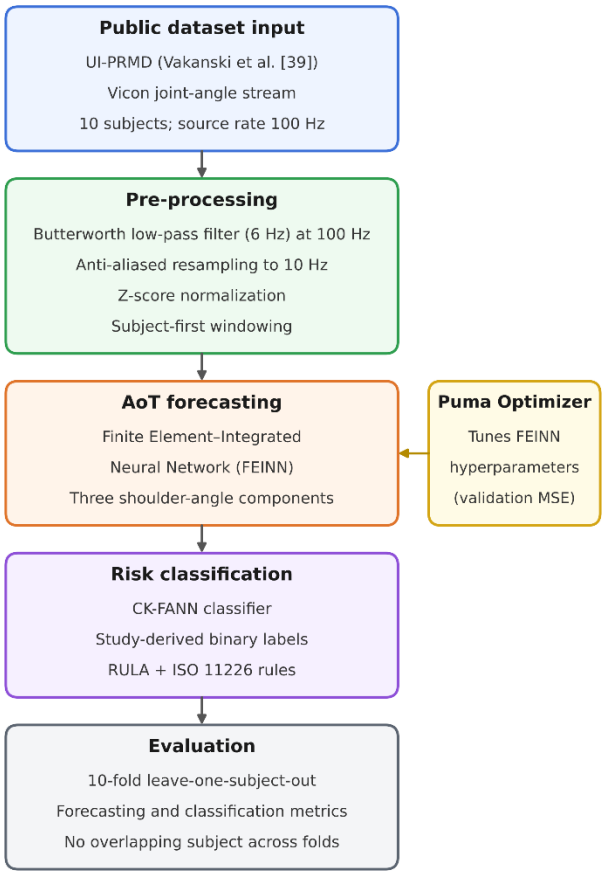


Fig. 1. FEPO-WMSDNet workflow for secondary analysis of UI-PRMD

Each component of FEPO-WMSDNet has a distinct intended role. FEM supplies displacement, strain, and stress relationships that act as a physical constraint on forecasting; FEINN integrates these relationships with the data-driven predictor; PO tunes selected FEINN hyperparameters; the convolutional stage extracts local temporal patterns from the forecast sequence; and the fractional-order stage performs adaptive binary risk classification. This modular rationale explains the design, but it does not establish the independent contribution of each component.

Because a component-wise ablation experiment was not performed, the present study evaluates and interprets the framework only as an integrated model.

3.1 UI-PRMD Dataset and Study Variables

This study used the publicly available University of Idaho Physical Rehabilitation Movements Dataset (UI-PRMD) introduced by Vakanski et al. [39]. No motion-capture experiment was conducted for the present study. The original dataset includes 10 healthy subjects, each performing 10 repetitions of 10 physical-rehabilitation movements. The movements are deep squat, hurdle step, inline lunge, side lunge, sit-to-stand, standing active straight-leg raise, standing shoulder abduction, standing shoulder extension, standing shoulder internal–external rotation, and standing shoulder scaption.

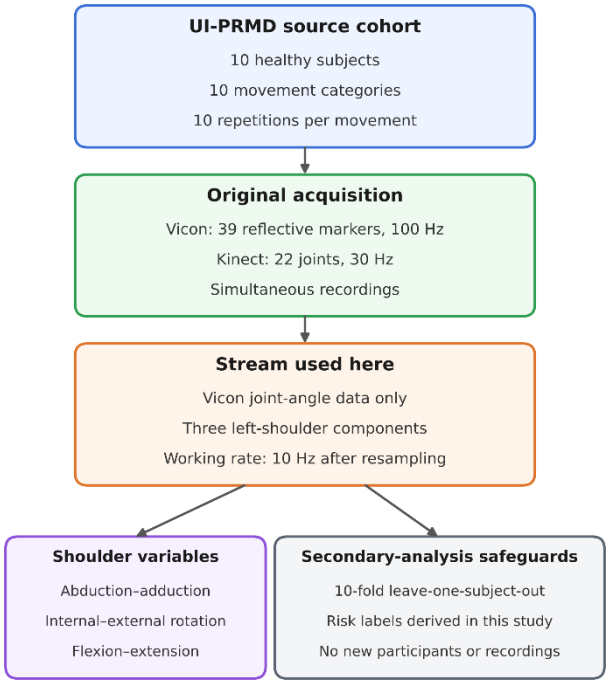


Fig. 2. UI-PRMD dataset profile and variables used in the present analysis

The original UI-PRMD study recorded the movements simultaneously with a Vicon optical motion-capture system and a Microsoft Kinect sensor. The Vicon stream used 39 reflective markers and was sampled at 100 Hz, whereas the Kinect stream contained 22 joints sampled at 30 Hz. Only the Vicon joint-angle data were used in the present analysis; the Kinect stream was not combined with the model input.

From the multivariate Vicon angle representation, the analysis retained three left-shoulder components: abduction–adduction, internal–external rotation, and flexion–extension. In the tables and figures, the labels "abduction–adduction," "internal–external rotation," and "flexion–extension" refer to these angular components and do not denote three UI-PRMD exercise categories.

The selected Vicon trajectories were processed at their original 100-Hz sampling rate and then converted to the 10-Hz working rate used by the forecasting pipeline. The 6-Hz smoothing filter described in Section 3.2.1 was applied at 100 Hz; conversion to 10 Hz used anti-aliased resampling so that the final bandwidth was consistent with the 5-Hz Nyquist limit. Accordingly, 100 Hz denotes the source frequency and 10 Hz denotes the post-resampling analysis frequency.

UI-PRMD provides movement recordings rather than clinical WMSD diagnoses or RULA/ISO risk annotations. The binary normal/risk targets used here were generated during this secondary analysis by applying the prespecified shoulder-angle and duration rules reported in **Table 3**. The resulting classes must therefore be interpreted as ergonomics-rule-derived labels, not as labels distributed with UI-PRMD.

Figure 2 summarizes the source dataset, the modality used, and the study variables. Because the source data are public and no new participants were recruited, the present work is a secondary analysis of existing human-motion recordings.

3.2 Data Pre-processing

The Vicon joint-angle trajectories were preprocessed to reduce measurement noise, correct short irregularities, and generate uniformly structured time-series inputs for forecasting and classification. All fold-dependent operations were fitted using training-subject data only.

3.2.1 Noise Removal and Signal Filtering

Optical motion-capture trajectories may contain high-frequency measurement noise or short gaps. A fourth-order low-pass Butterworth filter with a 6-Hz cutoff was applied to the selected 100-Hz Vicon angle channels, as represented in Eq. 1. Anti-aliasing was then applied during resampling to the 10-Hz working rate.

$$x_f(t) = \Im^{-1}\left[\frac{1}{\sqrt{1+\left(\frac{f}{f_c}\right)^{2n}}}\,\Im\big(x(t)\big)\right] \qquad (1)$$

where $x(t)$ is the raw motion signal, $x_f(t)$ is the filtered signal, $\Im$ and $\Im^{-1}$ denote the Fourier and inverse Fourier transforms, f is the frequency, f_c = 6 Hz is the cutoff frequency, and n = 4 is the filter order. This step reduces measurement noise in the internal–external rotation, abduction–adduction, and flexion–extension trajectories while retaining their temporal characteristics.

3.2.2 Data Normalization

Z-score normalization was used because the

three shoulder-angle components have different numerical ranges. Each feature was standardized according to Eq. 2 using statistics estimated only from the training subjects in each validation fold.

$$\tilde{x} = \frac{x - \mu}{\sigma} \quad (2)$$

where x denotes the original sample, $\tilde{x}$ is the normalized sample, μ is the training-set mean, and σ is the training-set standard deviation. This transformation centers each channel at zero with unit variance, which improves numerical stability during training.

3.2.3 Segmentation and Windowing

To capture temporal dependencies in sequential motion data, the preprocessed continuous time series were split into overlapping time frames. For AoT forecasting, the model forecasts future samples (H) based on a set number of samples (K) that represent the historical context in each window. The segmentation process is defined in Eq. 3.

$$X_i = [x_i, x_{i+1}, \dots, x_{i+K-1}]$$
$$Y_i = [x_{i+K}, x_{i+K+1}, \dots, x_{i+K+H-1}] \quad (3)$$

where X_i denotes the historical input sequence, Y_i denotes the forecast target, K is the look-back window length (256 samples), and H is the prediction horizon (10–40 samples).

Each input window contained 256 samples (25.6 s at 10 Hz). Adjacent windows were separated by 128 samples (12.8 s), giving 50% overlap. Forecast horizons of 1, 2, 3, and 4 s therefore corresponded to 10, 20, 30, and 40 future samples, respectively. Windows were generated within individual subject-movement recordings and never concatenated data from different subjects or movement files.

3.2.4 Missing-Sample Correction and Data Balancing

Cubic-spline interpolation was used to correct occasional missing or misaligned samples within a recording. Temporal warping and Gaussian-noise injection were used to reduce imbalance in the study-derived normal/risk classes. Augmentation was restricted to the training portion of each fold; no augmented sample from a held-out subject was used for model development.

3.2.5 Final Dataset Formation

After filtering, normalization, segmentation, and training-only augmentation, the sequences were represented as tensors of shape (N, 256, 3), where N is the number of windows, 256 is the window length, and 3 denotes the selected shoulder-angle components. These tensors formed the FEINN input for AoT forecasting.

3.2.6 Subject-Level Cross-Validation and Leakage Control

Generalization was evaluated using 10-fold leave-one-subject-out (LOSO) cross-validation. In each outer fold, recordings from nine UI-PRMD subjects were available for model development and the remaining subject was held out for testing. Subject assignment preceded window generation, normalization, interpolation, and augmentation. Training-subject statistics were applied unchanged to the test subject, and any validation data used for PO or early stopping were selected only from the training subjects. The held-out subject was not used for hyperparameter selection, checkpoint selection, or augmentation. This protocol prevents subject and overlapping-window leakage.

3.3 Prediction: Finite Element–Integrated Neural Network (FEINN)

FEINN [26] is the forecasting component of FEPO-WMSDNet. It combines the data-driven capacity of a deep neural network with finite-element equilibrium and boundary constraints so that future upper-limb trajectories are predicted while accounting for displacement, strain, and stress relationships. This differs from an unconstrained forecasting network, which learns only statistical associations in the observed trajectories.

3.3.1 Input-Output Representation

The motion capture points' spatial locations are represented by nodal coordinates in FEINN, which are used as network inputs. The coordinates for a two-dimensional domain are written as (x, y). The expected nodal displacements in both x- and y-directions,

represented by u_x^{NN} and u_y^{NN}, match the neural network output. One way to characterize the relationship is given in Eq. 4.

$$u_{\mathrm{NN}} = \begin{pmatrix} u_x^{\mathrm{NN}} \\ u_y^{\mathrm{NN}} \end{pmatrix} = \mathrm{DNN}(x, y \mid W) \tag{4}$$

where u_{NN} indicates the predicted nodal displacement vector from the neural network, u_x^{NN}, u_y^{NN} indicates the displacement components in x and y directions, $\mathrm{DNN}(\cdot)$ indicates the deep neural network function, (x, y) indicates the nodal coordinate values, and W indicates the trainable weight parameters of the neural network. This output captures the expected deformation pattern of the limb at each node for a given posture, forming the foundation for stress and strain computation.

3.3.2 Strain Computation

After nodal displacements are predicted, element strain is computed at the Gauss integration points using the strain–displacement matrix (B-matrix) derived from the finite-element shape functions, as shown in Eq. 5.

$$\{\varepsilon_{\mathrm{NN}}^{\mathrm{Gauss}}\} = [B]\{u_{\mathrm{NN}}\} \tag{5}$$

where $\{\varepsilon_{\mathrm{NN}}^{\mathrm{Gauss}}\}$ indicates the predicted strain vector at the Gauss point, $[B]$ indicates the strain–displacement matrix derived from the finite element shape functions, and $\{u_{\mathrm{NN}}\}$ indicates the predicted nodal displacement vector. This step is vital for biomechanical risk assessment.

3.3.3 Stress Computation

Hooke's law relates strain to stress through the constitutive matrix $[D]$, as shown in Eq. 6.

$$\{\sigma_{\mathrm{NN}}^{\mathrm{Gauss}}\} = [D]\{\varepsilon_{\mathrm{NN}}^{\mathrm{Gauss}}\} \tag{6}$$

where $\{\sigma_{\mathrm{NN}}^{\mathrm{Gauss}}\}$ indicates the predicted stress vector at the Gauss point, $[D]$ indicates the constitutive matrix, typically defined by Young's modulus E, and Poisson's ratio ν, and $\{\varepsilon_{\mathrm{NN}}^{\mathrm{Gauss}}\}$ indicates the strain vector from Eq. 5. This computation ensures that FEINN not only learns movement dynamics but also models internal mechanical loads, enabling a more realistic prediction of muscular stress contributing to WMSD risk.

3.3.4 Loss Function

The FEINN objective combines a forecasting (data) loss with internal force equilibrium and displacement boundary constraints. The total loss therefore penalizes the forecasting error, the difference between predicted internal and applied forces, and violations of the prescribed displacement conditions, as defined in Eqs. 7–9.

$$L_1 = \frac{1}{N_{\mathrm{node}}} \sum_{i=1}^{N_{\mathrm{node}}} \left\| F_{\mathrm{NN}}(x_i, y_i) - F_s(x_i, y_i) \right\|^2 \tag{7}$$

$$L_2 = \frac{1}{N_\Gamma} \sum_{i \in \Gamma} \left\| u_{\mathrm{NN}}(x_i, y_i) - u_\Gamma(x_i, y_i) \right\|^2 \tag{8}$$

$$L_{\mathrm{total}} = L_{\mathrm{data}} + w_1 L_1 + w_2 L_2 \tag{9}$$

where L_1 indicates the internal force equilibrium loss, L_{data} is the forecasting (data) loss on the predicted shoulder-angle trajectories, L_2 indicates the boundary displacement constraint loss, F_{NN} indicates the predicted internal force vector computed by FEM from neural network displacement outputs, F_s indicates the known external or body force vector, u_{NN} indicates the predicted nodal displacement vector from the neural network, u_Γ indicates the known displacement boundary conditions, N_{node} indicates the total number of discretized nodes, Γ is the set of boundary nodes with prescribed displacements, N_Γ is the number of those nodes, and w_1, w_2 indicate the weighting factors that balance the contributions of each loss term.

By using gradient descent to minimize L_{total}, the model can converge toward a solution that fulfills both learning accuracy and physical consistency.

3.3.5 Convergence Criterion

FEINN training monitored the relative change in the predicted force or displacement vector between successive iterations. Equation 10 defines the convergence measure used together with validation-based early stopping and the maximum-epoch limit.

$$\mathrm{Convergence} = \frac{\|x_{n+1} - x_n\|}{\|x_n\|} < \varepsilon \tag{10}$$

where x_n indicates the predicted force or displacement vector at the n^{th} iteration, x_{n+1} indicates the corresponding vector at iteration

$n+1$, ε indicates the convergence threshold. When the relative variation falls below ε, the convergence criterion is satisfied; training remains subject to the validation-based stopping rule and 100-epoch cap described in Section 3.3.7.

3.3.6 Architectural Configuration

FEINN uses a residual fully connected architecture with five hidden layers, four residual blocks, 120 neurons per layer, and tanh activations. The selected model uses a dropout rate of 0.30 and an L2 regularization coefficient of 1×10^{-4}; nodal coordinates are scaled to $[-1, 1]$. PO tunes the selected hyperparameters exclusively within the training data.

3.3.7 FEINN Training Configuration

FEINN was trained with Adam using a base learning rate of 0.001, a batch size of 32, and a maximum of 100 epochs. The total objective combined the forecasting loss with the weighted finite-element equilibrium and boundary-condition losses. Within the training portion of each LOSO fold, PO selected the learning rate, batch size, dropout rate, L2 regularization, and network depth using validation MSE. Early stopping was triggered when validation loss failed to improve for 10 consecutive epochs, and the checkpoint with the lowest validation loss was retained for evaluation on the held-out subject.

3.4 Hyperparameter Tuning using PO

The Puma Optimizer (PO) [27] was used to tune selected FEINN hyperparameters. PO is a population-based metaheuristic inspired by puma hunting and territorial behavior. Its exploration and exploitation stages search candidate learning rates, batch sizes, dropout rates, regularization coefficients, and network depths using validation MSE as the fitness criterion.

Step 1: Initialization

Initializing a population of possible hyperparameter sets, represented by X_i, each of which represents a puma in the search area, is the first step in the optimization process. While the other solutions function as female pumas investigating the search domain, the top-performing solution is regarded as the male puma.

PO evaluates each candidate using FEINN validation mean squared error as the fitness function. The objective is defined in Eq. 11.

$$f(X_i) = \frac{1}{N_{\text{val}}} \sum_{j=1}^{N_{\text{val}}} \left(\hat{y}_j - y_j\right)^2 \tag{11}$$

where N_{val} indicates the number of samples in validation data, y_j indicates the true output, and $\hat{y}_j$ indicates the predicted output from FEINN with parameters X_i. By iteratively updating the candidate hyperparameter vectors, the optimizer seeks to minimize this function.

Step 2: Phase Change Mechanism

PO alternates between exploration of new candidate regions and exploitation around the best-known candidates. The phase scores in Eqs. 12–15 determine which update mechanism is applied at each iteration.

$$\text{Score}_{\text{Explore}} = PF_1 \times f_1^{\text{Explore}} + PF_2 \times f_2^{\text{Explore}} \tag{12}$$

$$\text{Score}_{\text{Exploit}} = PF_1 \times f_1^{\text{Exploit}} + PF_2 \times f_2^{\text{Exploit}} \tag{13}$$

If $\text{Score}_{\text{Exploit}} \geq \text{Score}_{\text{Explore}}$, the algorithm enters the exploitation phase; otherwise it remains in exploration. Here, f_1, f_2 measure the rate at which cost values (model performance) improve between iterations, while PF_1 and PF_2 are control parameters that weigh the contributions of the two scoring functions; f_1 is defined in Eqs. 14 and 15.

$$f_1^{\text{Explore}} = PF_1 \frac{\text{Cost}_{\text{Initial}}^{\text{Best}} - \text{Cost}_{\text{Explore}}^{1}}{\text{SeqTime}} \tag{14}$$

$$f_1^{\text{Exploit}} = PF_1 \frac{\text{Cost}_{\text{Initial}}^{\text{Best}} - \text{Cost}_{\text{Exploit}}^{1}}{\text{SeqTime}} \tag{15}$$

where $\text{Cost}_{\text{Initial}}^{\text{Best}}$ indicates the cost of the best initial model, $\text{Cost}_{\text{Explore}}^{1}$, $\text{Cost}_{\text{Exploit}}^{1}$ indicates the costs in exploration and exploitation phases at iteration 1, and SeqTime indicates a constant parameter. This mechanism ensures that the optimizer intelligently transitions between global search and local refinement, improving convergence speed and avoiding local minima.

Step 3: Exploration Phase

During exploration, candidate hyperparameter vectors are perturbed across the specified search bounds to maintain population diversity and reduce premature convergence, as defined in Eq. 16.

$$\begin{gathered} Z_{i,G} = R_{\mathrm{Dim}}(U_b - L_b) + L_b, \\ \text{if } \mathrm{rand}_1 > 0.5; \\ Z_{i,G} = X_{a,G} + G\left(X_{a,G} - X_{b,G}\right) + G\,\Delta_G, \\ \text{otherwise, with} \\ \Delta_G = \left(X_{a,G} - X_{b,G}\right) - \left(X_{c,G} - X_{d,G}\right) \\ +\left(X_{c,G} - X_{d,G}\right) - \left(X_{e,G} - X_{f,G}\right) \end{gathered} \tag{16}$$

where U_b and L_b are the upper and lower search bounds; R_{Dim} is a random vector in [0, 1]; $X_{a,G}$ through $X_{f,G}$ are randomly selected population members; rand_1 is uniformly distributed in [0, 1]; G controls the exploration perturbation; Δ_G is the combined difference term of the second branch; and $Z_{i,G}$ is the resulting candidate for puma i, which is accepted only through the selection rule in Eq. 18. This operator diversifies the candidate population and reduces premature convergence.

Step 4: Exploitation Phase

During exploitation, the ambush and sprint operators concentrate the search around promising candidates while retaining stochastic perturbations, as defined in Eq. 17.

$$\begin{gathered} X_{\mathrm{new}} = \left(\frac{\mathrm{mean}\left(\mathrm{Sol}_{\mathrm{total}}\right)}{N_{\mathrm{pop}}}\right) X_{r1} - \frac{(-1)^b X_i}{1 + a\,\mathrm{rand}_5}, \\ \text{if } \mathrm{rand}_4 \geq 0.5; \\ X_{\mathrm{new}} = \mathrm{Puma}_{\mathrm{male}} + 2\,\mathrm{rand}_7 \exp\left(\mathrm{randn}_1\right) \\ \times (X_{r2} - X_i), \quad \text{else if } \mathrm{rand}_6 \geq L; \\ X_{\mathrm{new}} = \frac{2\,\mathrm{rand}_8\left[F_1 R X_i + F_2\left(1 - R\right)\mathrm{Puma}_{\mathrm{male}}\right]}{\left(2\,\mathrm{rand}_9 - 1 + \mathrm{randn}_2\right) - \mathrm{Puma}_{\mathrm{male}}}, \\ \text{otherwise.} \end{gathered} \tag{17}$$

where $\mathrm{Puma}_{\mathrm{male}}$ is the best current solution; X_i is the current solution; X_{r1} and X_{r2} are randomly selected solutions; a, b, and L are control parameters; rand_4–rand_9 are uniform random variables; randn_1 and randn_2 are normally distributed perturbations; $\mathrm{Sol}_{\mathrm{total}}$ is the sum of the current solutions; N_{pop} is the population size; and R, F_1, and F_2 are weighting terms. The three branches represent sprint and ambush updates around promising solutions.

Step 5: Parameter Update and Selection

After each iteration, a new candidate replaces the current candidate only when it produces a lower validation cost, according to the greedy selection rule in Eq. 18.

$$X_i = X_{\mathrm{new}}, \quad \text{if } \mathrm{Cost}(X_{\mathrm{new}}) < \mathrm{Cost}(X_i) \tag{18}$$

where X_{new} is the candidate generated by Eq. 16 or Eq. 17. This selection rule retains improved hyperparameter combinations while the exploration mechanism preserves diversity in the candidate population.

Step 6: Convergence and Optimal Hyperparameters

Optimization continues until the maximum number of iterations is reached or improvement falls below the specified threshold. Equation 19 defines the convergence measure.

$$\mathrm{Convergence} = \frac{\left|\mathrm{Cost}_{n+1} - \mathrm{Cost}_n\right|}{\left|\mathrm{Cost}_n\right|} < \varepsilon \tag{19}$$

where ε indicates the small threshold ensuring stable and precise convergence. Upon completion, the best hyperparameter configuration is adopted for training the FEINN model, achieving an optimal balance between accuracy, training stability, and generalization capability. The step-by-step process of parameter optimization is given in Figure 3.

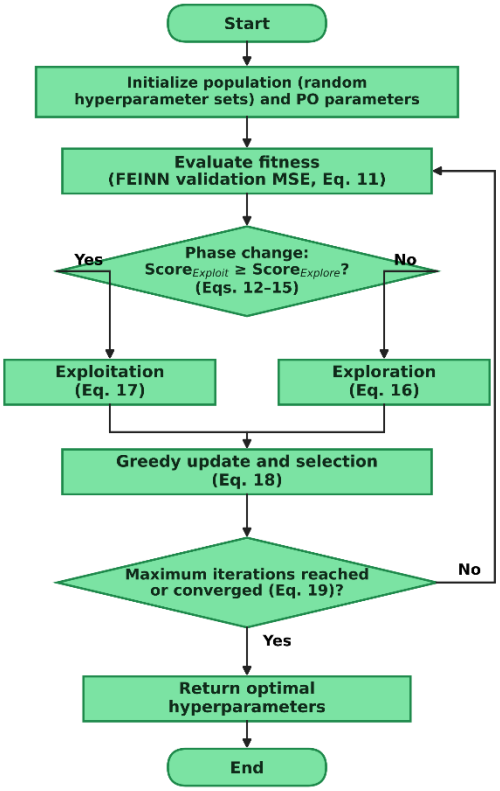


Fig. 3. Puma Optimizer hyperparameter-search workflow

Step 7: Integration in FEPO-WMSDNet

Within FEPO-WMSDNet, PO tunes the learning rate, dropout rate, batch size, L2 regularization coefficient, and network depth to minimize validation loss, as summarized in Eq. 20 and **Table 4**. The selected architecture used five hidden layers, as reported in **Table 4**.

$$\min_{\eta, p, N_B, \lambda, n_h} f(\eta, p, N_B, \lambda, n_h) \tag{20}$$

where η is the learning rate, p is the dropout rate, N_B is the batch size, λ is the L2 regularization coefficient, n_h is the number of hidden layers (network depth), and f is the validation MSE defined in Eq. 11.

This optimization stage is intended to improve convergence and reduce validation error; its contribution is not interpreted independently because the present study did not include a component-wise ablation experiment.

3.5 Risk Classification Using CK-FANN

CK-FANN classifies the predicted upper-limb motion windows as normal or risk. It combines convolutional feature extraction with the Karcı fractional-order learning mechanism [28] to model nonlinear temporal patterns in the forecast shoulder-angle sequences.

Conventional neural networks update their weights using first-order gradients scaled by an optimizer learning rate. CK-FANN retains Adam with a base learning rate of 0.001 but replaces the ordinary derivative term in the backpropagated update with the Karcı fractional derivative. The fractional term therefore adapts the effective update magnitude; it does not eliminate the optimizer's base learning-rate parameter.

The fractional-order term introduces a memory-like dependence on the current error and weight state, which is intended to stabilize convergence. Equation 21 defines the fractional derivative used in the update rule.

$$D_K^{\alpha} f(x) = \left(\frac{f(x)}{x}\right)^{\alpha-1} \cdot f'(x) \tag{21}$$

where D_K^{α} denotes the Karcı fractional derivative of order α, with $\alpha \in (0, 1]$, f is a differentiable function, and f' is its ordinary first derivative. The fractional order changes the effective update in response to the error and weight state. FEINN forecasts provide the motion features used to train CK-FANN. Training used Adam, binary cross-entropy, a batch size of 32, a maximum of 100 epochs, and early-stopping patience of 10 epochs; the checkpoint with the lowest training-subject validation loss was retained.

3.5.1 Convolutional Feature Extraction

Convolutional layers process the three forecast shoulder-angle channels to extract discriminative temporal features before classification. The feature-map output of each convolutional layer is defined in Eq. 22.

$$F_o^{(l)}(i,j) = \varphi\left(\sum_{k=1}^{n} W^{(l)}(j,k) * F_o^{(l-1)}(i,k) + b^{(l)}(j)\right) \tag{22}$$

where $F_o^{(l)}(i,j)$ is the output of feature map j at position i in layer l, $W^{(l)}(j,k)$ is the convolution kernel connecting input channel k to feature map j, $b^{(l)}(j)$ is the bias, n is the number of input channels, φ is the activation function, and * denotes convolution. The resulting feature maps are flattened and passed to the fractional-learning layers.

3.5.2 Fractional Weight Update Mechanism

By adding Karcı fractional derivatives to the weight update procedure, CK-FANN alters the conventional backpropagation rule. The weight update rule for each layer is given in Eq. 23. Binary cross-entropy was used as the classification loss.

$$W_{\text{new}}^{(l)} = W^{(l)} - \eta\, D_K^{\alpha} E\left(W^{(l)}\right) \tag{23}$$

where $W^{(l)}$ is the weight matrix in layer l, η is the base learning rate (0.001), E is the binary cross-entropy loss, and $D_K^{\alpha} E\left(W^{(l)}\right)$ is the Karcı fractional derivative of E with respect to $W^{(l)}$ (Eqs. 25–27), used in place of the ordinary gradient. For n binary samples, the classification loss is defined in Eq. 24.

$$E = -\frac{1}{n}\sum_{i=1}^{n}\left[O_i \ln\left(\hat{O}_i\right) + (1-O_i)\ln\left(1-\hat{O}_i\right)\right] \tag{24}$$

where O_i is the true binary label (0 for normal and 1 for risk) and $\hat{O}_i$ is the predicted risk probability.

3.5.3 Fractional Gradient Calculation for Output Layer

The output-layer weight adjustment is calculated with the fractional derivative in Eq. 25.

$$D_K^{\alpha} E_{W^{(3)}} = \left(\frac{E}{W^{(3)}}\right)^{\alpha-1} \frac{\partial E}{\partial F_o^{(3)}} \cdot \frac{\partial F_o^{(3)}}{\partial F^{(3)}} \cdot \frac{\partial F^{(3)}}{\partial W^{(3)}} \tag{25}$$

where $F^{(3)}$ is the output-layer pre-activation, $F_o^{(3)}$ is the post-activation output, $W^{(3)}$ is the output-layer weight matrix, and α is the fractional order controlling the update magnitude.

3.5.4 Fractional Backpropagation for Hidden Layers

Fractional derivatives are recursively applied to the hidden-layer updates, as shown in Eq. 26.

$$D_K^{\alpha} E_{W^{(2)}} = \left(\frac{E}{W^{(2)}}\right)^{\alpha-1} \frac{\partial E}{\partial F_o^{(3)}} \cdot \frac{\partial F_o^{(3)}}{\partial F^{(3)}} \cdot \frac{\partial F^{(3)}}{\partial F_o^{(2)}} \cdot \frac{\partial F_o^{(2)}}{\partial F^{(2)}} \cdot \frac{\partial F^{(2)}}{\partial W^{(2)}} \tag{26}$$

The corresponding input-layer update is given in Eq. 27.

$$D_K^{\alpha} E_{W^{(1)}} = \left(\frac{E}{W^{(1)}}\right)^{\alpha-1} \frac{\partial E}{\partial F_o^{(3)}} \cdot \frac{\partial F_o^{(3)}}{\partial F^{(3)}} \cdot \frac{\partial F^{(3)}}{\partial F_o^{(2)}} \cdot \frac{\partial F_o^{(2)}}{\partial F^{(2)}} \cdot \frac{\partial F^{(2)}}{\partial F_o^{(1)}} \cdot \frac{\partial F_o^{(1)}}{\partial F^{(1)}} \cdot \frac{\partial F^{(1)}}{\partial W^{(1)}} \tag{27}$$

The recursive fractional derivatives are applied through the hidden and input layers to update CK-FANN weights.

3.5.5 Binary Risk Classification and Decision Function

After training, CK-FANN converts its output to a risk probability using Eq. 28 and assigns the binary class using Eq. 29.

$$P_{\text{risk}} = \sigma\left(F^{(3)}\right) = \frac{1}{1+e^{-F^{(3)}}}, \quad P_{\text{risk}} \in [0,1] \tag{28}$$

$$\text{Class} = \begin{cases} \text{Normal}, & \text{if } P_{\text{risk}} < \tau \\ \text{Risk}, & \text{if } P_{\text{risk}} \geq \tau \end{cases} \tag{29}$$

where τ is the decision threshold, set to 0.5 in this study (Table 4).

Table 3. Study-derived WMSD-risk rules applied to UI-PRMD shoulder angles (based on RULA and ISO 11226)

Shoulder angle component	Angular threshold (°)	Risk duration (s)	Equivalent samples at 10 Hz
Internal–external rotation	$\lvert\theta_{i,t}\rvert > 15°$	4	40
Abduction–adduction	$\theta_{i,t} > 40°$	4	40
Flexion–extension	$\theta_{i,t} > 40°$	4	40

In Table 3, $\theta_{i,t}$ denotes the angle of shoulder component i at sample t. **Table 3** defines the study-derived rules used to generate binary risk targets from the selected UI-PRMD shoulder-angle trajectories; these labels are not supplied with UI-PRMD. A window was assigned to the risk class when the relevant angle exceeded its threshold for more than 4 s (40 samples at 10 Hz); otherwise it was assigned to the normal class. CK-FANN was trained in batches of 32 with binary cross-entropy loss, and the checkpoint with the lowest training-subject validation loss was retained.

4 Results and Discussion

The proposed FEPO-WMSDNet was evaluated for two tasks: AoT forecasting of the three selected Vicon shoulder-angle components and classification of the study-derived normal/risk targets. The source data were the UI-PRMD Vicon joint-angle recordings, originally sampled at 100 Hz and resampled to 10 Hz for analysis. The model was implemented in TensorFlow with Python 3.11 and trained on an Intel Xeon 1.70-GHz workstation with 56 CPU cores and 2 TB of storage. Training used Adam, an initial learning rate of 0.001, a batch size of 32, a maximum of 100 epochs, validation-loss early stopping, dropout, and L2 regularization. Forecasting was evaluated with R^2, RMSE, MAE, and MAPE; classification was evaluated with MCC, accuracy, F1-score, precision, recall, and specificity. The experimental baselines were SVM-XG-MLP-LSTM-Naïve-WMSDNet [23], ANN-WMSDNet [24], and LR-SVM-DT-RF-XGBoost-WMSDNet [25]. **Table 4** lists the parameter settings.

Table 4. Model, preprocessing, and implementation parameters

Module	Hyperparameter	Value
Dataset	Source dataset	UI-PRMD (Vakanski et al. [39])
	Number of subjects	10
	Source protocol	10 movements; 10 repetitions per movement per subject
	Modality analyzed	Vicon joint-angle data (39-marker source stream)
	Selected variables	Left shoulder: flexion–extension, abduction–adduction, internal–external rotation
	Working sampling frequency	10 Hz (after resampling)
	Original Vicon sampling frequency	100 Hz
	Validation strategy	Leave-one-subject-out cross-validation (10 folds)
	Training subjects per fold	9
	Testing subjects per fold	1
Data Pre-processing	Signal filter	Butterworth low-pass filter
	Data normalization	Z-score
	Cutoff frequency	6 Hz at the 100-Hz source rate; anti-aliased resampling to 10 Hz
	Filter order	4
	Window overlap	50%
	Window stride	128 samples
	Window length	256 samples
	Missing value correction	Cubic-spline interpolation
	Forecast horizons	10, 20, 30, and 40 samples (1–4 s)
	Data augmentation	Gaussian-noise injection, temporal warping
	Input tensor shape	(N, 256, 3)
FEINN	Neurons per layer	120
	Residual blocks	4
	Hidden layers	5
	Network architecture	Residual fully connected neural network
	Maximum epochs	100
	Batch size	32
	Initial learning rate	0.001
	Activation function	tanh
	Convergence threshold	1×10^{-6}
	Early stopping patience	10 epochs without validation-loss improvement
	Dropout rate	0.30
	L2 regularization	1×10^{-4}
Puma Optimizer	Population size	30
	Maximum iterations	100
	Fitness function	Validation MSE
	Optimized hyperparameters	Learning rate, batch size, dropout rate, L2 regularization, and network depth

	Stopping criteria	Convergence threshold
CK-FANN	Input	FEINN forecasted motion features
	Fractional learning	Karcı fractional derivative within Adam-based training
	Convolutional feature extraction	Enabled
	Output layer	Binary classification
	Batch size	32
	Learning rate	0.001
	Output activation	Sigmoid
	Classification threshold	0.50
Study-derived labels	Ergonomic assessment standards	RULA + ISO 11226
	Rotation threshold	> 15° for 4 s
	Flexion threshold	> 40° for 4 s
	Abduction threshold	> 40° for 4 s
Implementation	Programming language	Python 3.11
	Framework	TensorFlow
	Hardware platform	Intel Xeon 1.70 GHz
	Storage	2 TB

4.1 Experimental Protocol and Dataset

Model stability was assessed over five independent runs performed under the same subject-level evaluation protocol. Metrics are reported as the mean and sample standard deviation across runs. Classification metrics are averaged across the three shoulder-angle components, with each metric averaged separately; accuracy, F1-score and MCC are therefore not recomputed from the averaged precision, recall and specificity and need not match values derived from them. The 95% confidence intervals in **Table 9** were calculated with the t distribution (n = 5 runs, df = 4). **Table 8** reports paired t-test comparisons across matched runs, whereas **Table 11** reports Wilcoxon signed-rank comparisons across matched LOSO subject folds. The reported p-values are unadjusted and should be interpreted as exploratory.

The evaluation used the public UI-PRMD dataset described in Section 3.1 and originally collected by Vakanski et al. [39]. UI-PRMD contains 10 healthy subjects and 10 repetitions of each of 10 rehabilitation movements, recorded with Vicon and Kinect. This study used only the Vicon joint-angle stream. The three analyzed channels were the left-shoulder abduction–adduction, internal–external rotation, and flexion–extension components; the component labels in Figures 4–6 and 10–22 refer to these components rather than to three exercise categories. The original 100-Hz Vicon trajectories were resampled to 10 Hz and evaluated with 10-fold LOSO cross-validation. In Figures 4–6, ds denotes deciseconds (10 samples per second). The dataset was partitioned by subject before temporal windows were generated. Because UI-PRMD is a rehabilitation dataset rather than an occupational cohort, the results assess algorithmic performance on a public motion benchmark and do not establish generalization to textile workers or other industrial populations.

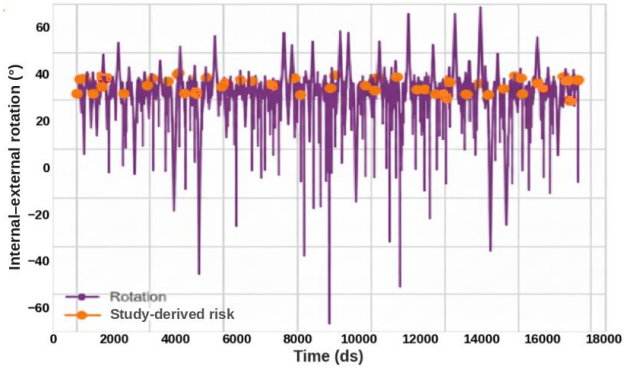


Fig. 4. Illustrative post-resampling shoulder internal–external rotation angle with study-derived risk windows (time in deciseconds)

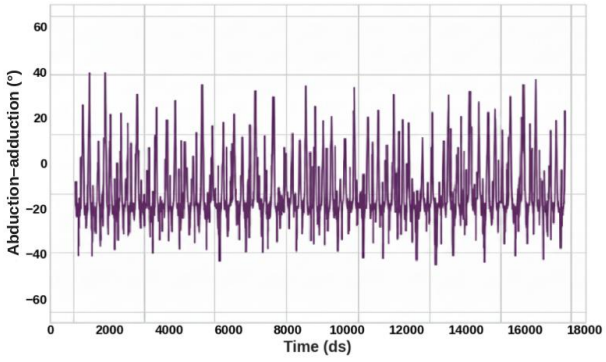


Fig. 5. Illustrative post-resampling shoulder abduction–adduction angle (time in deciseconds)

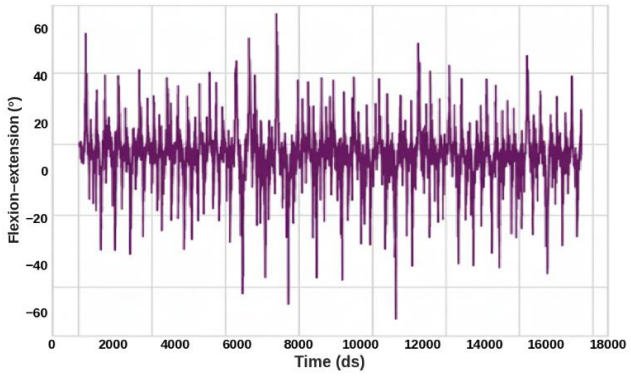


Fig. 6. Illustrative post-resampling shoulder flexion–extension angle (time in deciseconds)

Figure 7 shows that the training and validation losses decreased in parallel and stabilized without a marked late-epoch divergence. Figure 8 presents the confusion matrix: 96.9% of risk samples and 98.2% of normal samples were correctly classified. Figure 9 presents the ROC curve (AUC = 0.977), providing a threshold-independent summary of discrimination. Together, these diagnostics complement the LOSO metrics but do not remove the limitations associated with the small number of independent subjects.

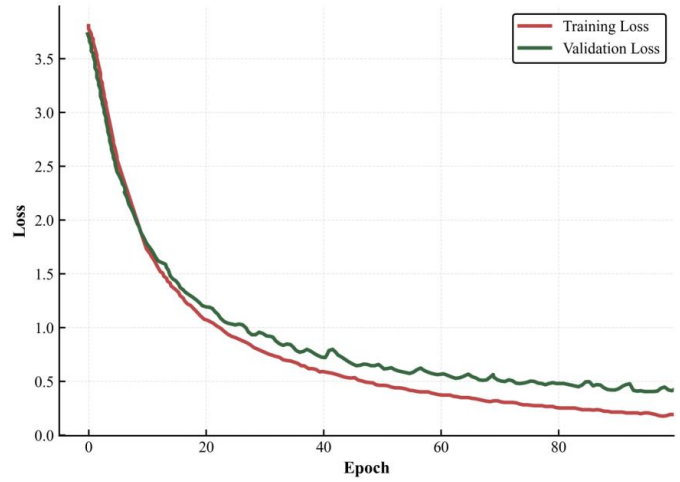


Fig. 7. Training and validation loss curves

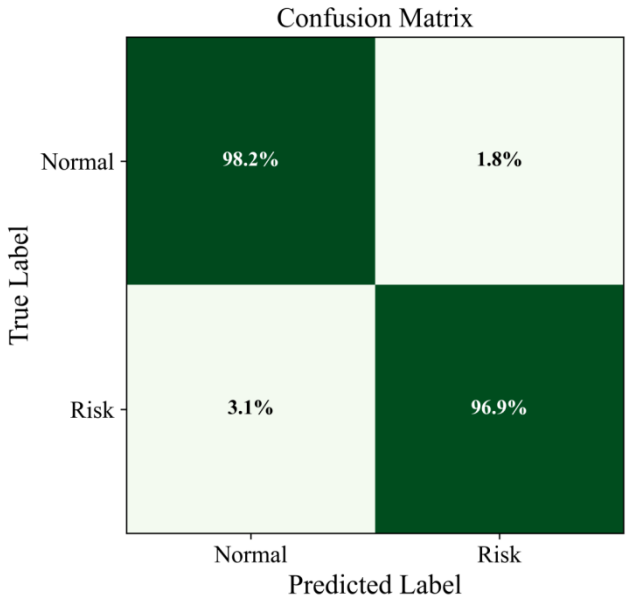


Fig. 8. Row-normalized confusion matrix for study-derived WMSD-risk classification, averaged across the three shoulder-angle components

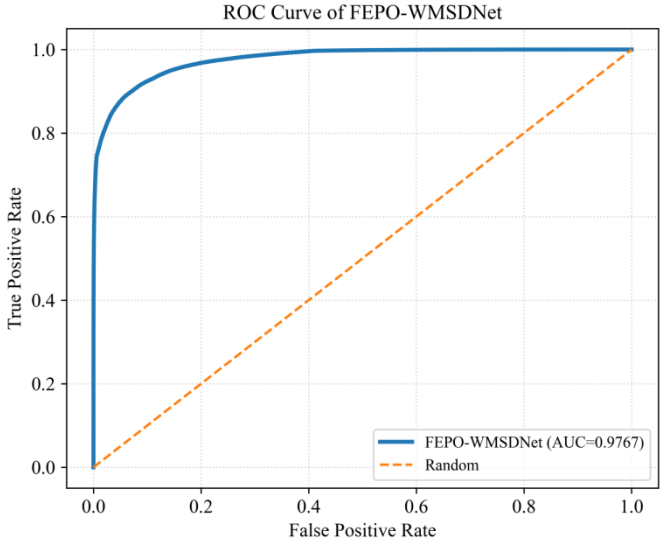


Fig. 9. Receiver operating characteristic curve for WMSD-risk classification

4.2 Performance Metrics

4.2.1 AoT Motion Angle Forecasting

Coefficient of determination (R^2): quantifies the proportion of variance in the true shoulder-angle values explained by the AoT forecasts and is calculated using Eq. 30.

$$R^2 = 1 - \frac{\sum_{k=1}^{Z}\left(A_{angle,k} - P_{angle,k}\right)^2}{\sum_{k=1}^{Z}\left(A_{angle,k} - Mean\right)^2} \qquad (30)$$

where Z denotes the number of evaluated

forecast samples in the fold, $A_{angle,k}$ is the true Vicon shoulder-angle value for sample k, $P_{angle,k}$ is the corresponding AoT forecast, and $Mean$ is the mean of the true angle values. The same symbols are used in Eqs. 31–33.

Root mean squared error (RMSE): measures the square root of the mean squared difference between the true and forecast shoulder angles and is calculated using Eq. 31.

$$RMSE = \sqrt{\frac{1}{Z}\sum_{k=1}^{Z}\left(A_{angle,k} - P_{angle,k}\right)^2} \quad (31)$$

Mean absolute error (MAE): measures the mean absolute difference between the true and forecast shoulder angles and is calculated using Eq. 32.

$$MAE = \frac{1}{Z}\sum_{k=1}^{Z}\left|A_{angle,k} - P_{angle,k}\right| \quad (32)$$

Mean absolute percentage error (MAPE): measures the mean percentage deviation of the forecast from the true shoulder angle and is calculated using Eq. 33. Because MAPE divides by the true angle, it is sensitive to samples whose true angle is close to zero and is interpreted together with RMSE and MAE.

$$MAPE = \frac{100}{Z}\sum_{k=1}^{Z}\left|\frac{A_{angle,k} - P_{angle,k}}{A_{angle,k}}\right| \quad (33)$$

4.2.2 WMSD-Risk Classification

Accuracy: the proportion of risk and normal samples classified correctly, calculated using Eq. 34.

$$Accuracy = \frac{TP + TN}{TP + TN + FP + FN} \quad (34)$$

Precision: the proportion of samples predicted as risk that were true risk samples, calculated using Eq. 35.

$$Precision = \frac{TP}{TP + FP} \quad (35)$$

Recall (sensitivity): the proportion of true risk samples correctly identified, calculated using Eq. 36.

$$Recall = \frac{TP}{TP + FN} \quad (36)$$

F1-score: the harmonic mean of precision and recall, calculated using Eq. 37.

$$F1 = 2 \times \frac{Precision \times Recall}{Precision + Recall} \quad (37)$$

Specificity: the proportion of true normal samples correctly identified, calculated using Eq. 38.

$$Specificity = \frac{TN}{TN + FP} \quad (38)$$

Matthews correlation coefficient (MCC): a balanced measure based on all four confusion-matrix outcomes, calculated using Eq. 39.

$$MCC = \frac{TP \times TN - FP \times FN}{\sqrt{D}}$$
$$D = (TP + FP)(TP + FN) \times (TN + FP)(TN + FN) \quad (39)$$

where TP (True Positive) denotes the number of times the model correctly predicted a risk event. TN (True Negative) denotes the number of times the model correctly predicted a normal event. FP (False Positive) denotes the number of times the model incorrectly predicted a risk event when the true event was normal. FN (False Negative) denotes the number of times the model incorrectly predicted a normal event when the true event was risk.

4.2.3 Cross-Subject Validation Results

Subject-level generalization was assessed using 10-fold LOSO cross-validation. Each fold trained the framework using nine UI-PRMD subjects and evaluated it on the subject excluded from model development and preprocessing-statistic estimation. **Table 5** reports each held-out subject's classification performance and the mean ± sample standard deviation across the 10 folds. This design limits subject leakage, although the small number of independent subjects remains an important limitation.

Table 5. LOSO classification performance by held-out subject (each metric averaged separately

across the three shoulder-angle components)

Test subject	Accuracy (%)	Recall (%)	Precision (%)	F1-score (%)	MCC
Subject 1	96.18	96.76	95.02	95.88	0.950
Subject 2	96.71	97.16	95.47	96.31	0.959
Subject 3	96.29	96.69	95.13	95.90	0.952
Subject 4	96.83	97.27	95.61	96.43	0.961
Subject 5	95.95	96.38	94.70	95.52	0.946
Subject 6	96.56	96.94	95.31	96.12	0.956
Subject 7	96.16	96.61	94.95	95.77	0.949
Subject 8	96.94	97.35	95.72	96.53	0.962
Subject 9	96.41	96.86	95.19	96.02	0.954
Subject 10	96.61	97.03	95.36	96.19	0.957
Mean ± SD	96.46 ± 0.32	96.90 ± 0.31	95.25 ± 0.31	96.07 ± 0.31	0.955 ± 0.005

4.3 Performance Analysis

4.3.1 AoT Motion Angle Forecasting

Figures 10–13 compare FEPO-WMSDNet with the three experimentally evaluated WMSD-specific baselines for AoT forecasting of the three selected shoulder-angle components: abduction–adduction, internal–external rotation, and flexion–extension. Table 6 lists the corresponding values.

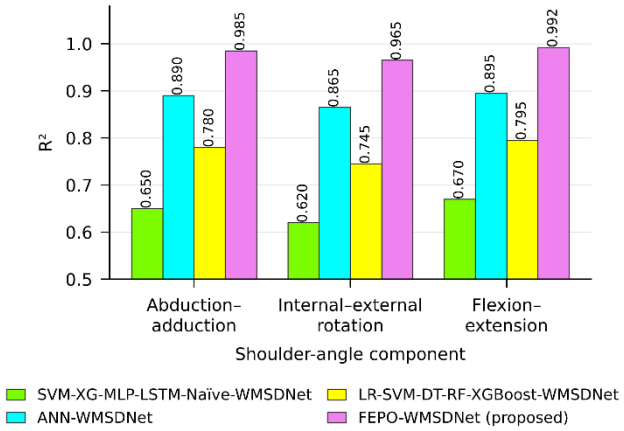


Fig. 10. R^2 comparison for AoT shoulder-angle forecasting

Figure 10 compares R^2 across the three shoulder-angle components. Relative to SVM-XG-MLP-LSTM-Naïve-WMSDNet, ANN-WMSDNet, and LR-SVM-DT-RF-XGBoost-WMSDNet, respectively, FEPO-WMSDNet reported R^2 increases of 51.54%, 10.67%, and 26.28% for abduction–adduction; 55.65%, 11.56%, and 29.53% for internal–external rotation; and 48.06%, 10.84%, and 24.78% for flexion–extension. These comparisons apply only to the evaluated baselines.

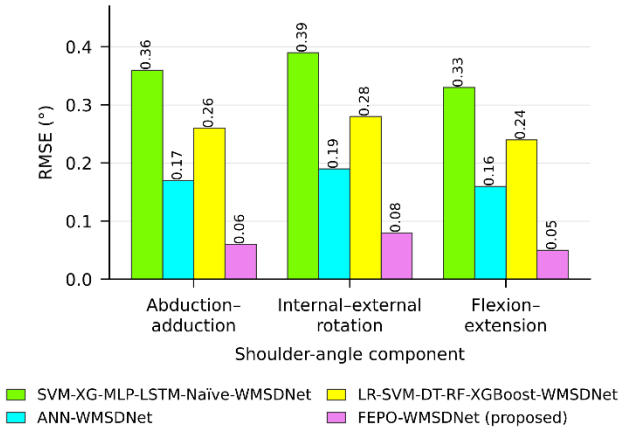


Fig. 11. RMSE comparison for AoT shoulder-angle forecasting

Figure 11 compares RMSE across the three shoulder-angle components. Relative to the same three baselines, FEPO-WMSDNet reported RMSE reductions of 83.33%, 64.71%, and 76.92% for abduction–adduction; 79.49%, 57.89%, and 71.43% for internal–external rotation; and 84.85%, 68.75%, and 79.17% for flexion–extension.

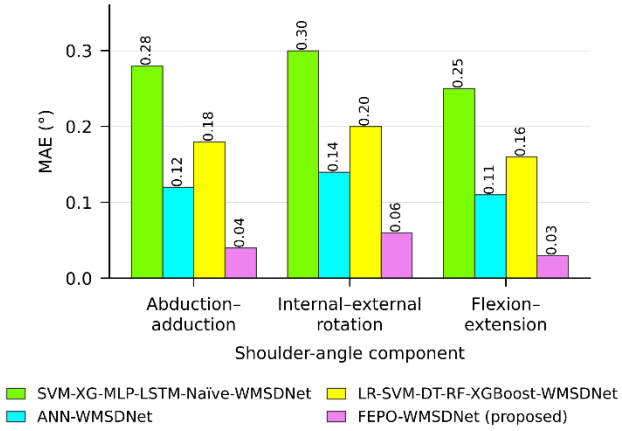


Fig. 12. MAE comparison for AoT shoulder-angle forecasting

Figure 12 compares MAE across the three shoulder-angle components. Relative to the same three baselines, FEPO-WMSDNet reported MAE reductions of 85.71%, 66.67%, and 77.78% for abduction–adduction; 80.00%, 57.14%, and 70.00% for internal–external rotation; and 88.00%, 72.73%, and 81.25% for flexion–extension.

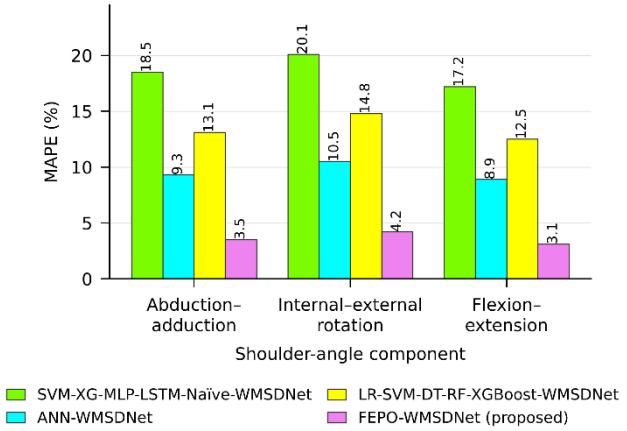


Fig. 13. MAPE comparison for AoT shoulder-angle forecasting

Figure 13 compares MAPE across the three shoulder-angle components. Relative to the same three baselines, FEPO-WMSDNet reported MAPE reductions of 81.08%, 62.37%, and 73.28% for abduction–adduction; 79.10%, 60.00%, and 71.62% for internal–external rotation; and 81.98%, 65.17%, and 75.20% for flexion–extension.

4.3.2 WMSD Risk Classification

Figures 14–19 compare FEPO-WMSDNet with the three experimentally evaluated WMSD-specific baselines for classification of the study-derived risk labels across the three selected shoulder-angle components: abduction–adduction, internal–external rotation, and flexion–extension. Table 7 summarizes the component-level results.

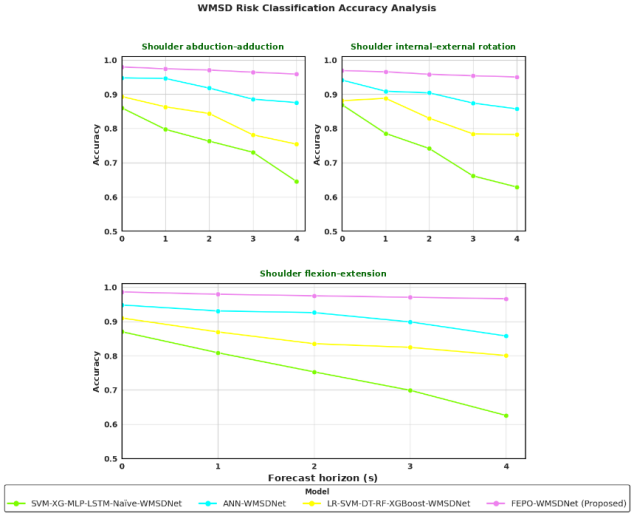


Fig. 14. Classification accuracy across AoT horizons for the three shoulder-angle components

Figure 14 presents accuracy across the 1–4-s AoT range. At 1 s, FEPO-WMSDNet reported accuracy improvements of 22.17%, 2.98%, and 11.10% for abduction–adduction; 22.87%, 6.24%, and 7.74% for internal–external rotation; and 21.12%, 5.24%, and 11.00% for flexion–extension relative to the three baselines, respectively. At 4 s, the corresponding improvements were 48.55%, 9.50%, and 27.11%; 51.04%, 10.86%, and 21.46%; and 54.46%, 12.66%, and 20.67%.

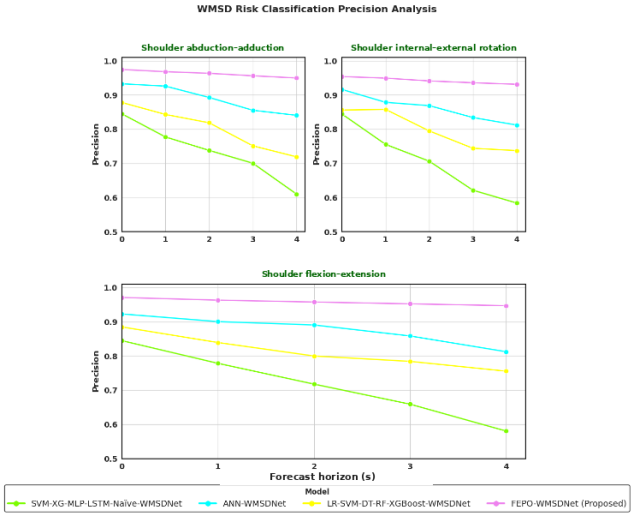


Fig. 15. Classification precision across AoT horizons for the three shoulder-angle components

Figure 15 presents precision across the 1–4-s AoT range. At 1 s, FEPO-WMSDNet reported improvements of 24.54%, 4.55%, and 12.51% for abduction–adduction; 25.63%, 8.04%, and

9.14% for internal–external rotation; and 23.74%, 6.97%, and 14.77% for flexion–extension. At 4 s, the corresponding improvements were 55.59%, 12.99%, and 32.05%; 59.42%, 14.66%, and 26.29%; and 63.16%, 16.56%, and 19.15%.

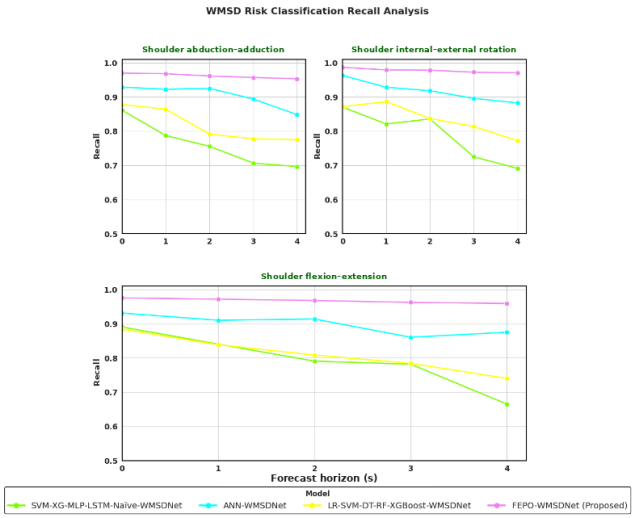


Fig. 16. Classification recall across AoT horizons for the three shoulder-angle components

Figure 16 presents recall across the 1–4-s AoT range. At 1 s, FEPO-WMSDNet reported improvements of 22.93%, 4.92%, and 10.38% for abduction–adduction; 19.24%, 5.45%, and 9.28% for internal–external rotation; and 15.64%, 6.77%, and 13.33% for flexion–extension. At 4 s, the corresponding improvements were 36.84%, 12.34%, and 22.99%; 40.36%, 9.95%, and 25.66%; and 44.23%, 9.61%, and 29.58%.

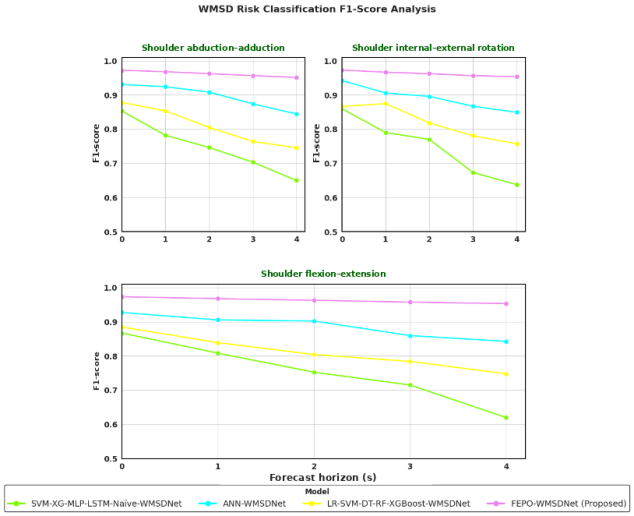


Fig. 17. Classification F1-score across AoT horizons for the three shoulder-angle components

Figure 17 presents F1-score across the 1–4-s AoT range. At 1 s, FEPO-WMSDNet reported improvements of 23.75%, 4.75%, and 11.46% for abduction–adduction; 22.49%, 6.77%, and 9.22% for internal–external rotation; and 19.71%, 6.87%, and 12.86% for flexion–extension. At 4 s, the corresponding improvements were 46.24%, 12.65%, and 27.52%; 50.11%, 12.36%, and 25.99%; and 53.75%, 13.11%, and 27.45%.

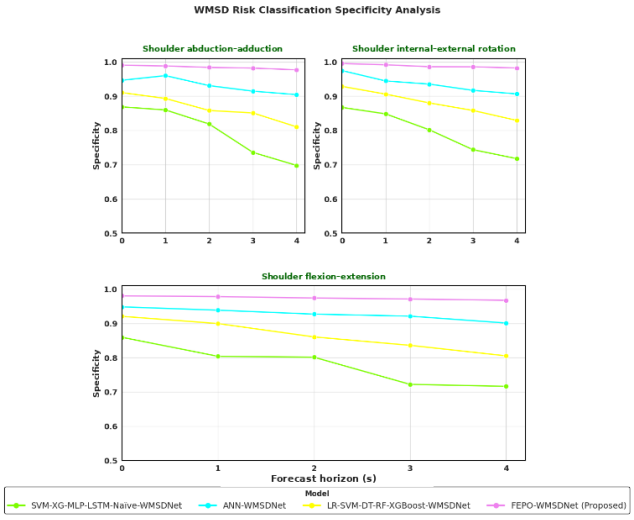


Fig. 18. Classification specificity across AoT horizons for the three shoulder-angle components

Figure 18 presents specificity across the 1–4-s AoT range. At 1 s, FEPO-WMSDNet reported improvements of 14.93%, 2.93%, and 9.49% for abduction–adduction; 16.88%, 4.98%, and

8.56% for internal–external rotation; and 21.66%, 4.21%, and 7.86% for flexion–extension. At 4 s, the corresponding improvements were 39.94%, 8.01%, and 20.51%; 36.83%, 8.35%, and 18.43%; and 35.05%, 7.36%, and 20.14%.

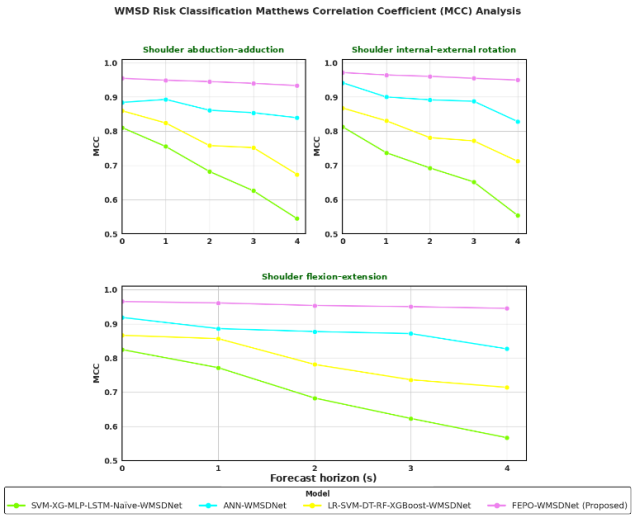


Fig. 19. Matthews correlation coefficient across AoT horizons for the three shoulder-angle components

Figure 19 presents MCC across the 1–4-s AoT range. At 1 s, FEPO-WMSDNet reported improvements of 25.66%, 6.28%, and 12.51% for abduction–adduction; 30.83%, 7.15%, and 13.39% for internal–external rotation; and 24.53%, 8.46%, and 10.44% for flexion–extension. At 4 s, the corresponding improvements were 71.41%, 11.21%, and 38.56%; 71.34%, 14.61%, and 33.33%; and 66.71%, 14.33%, and 32.34%. These benchmark comparisons do not by themselves establish workplace effectiveness.

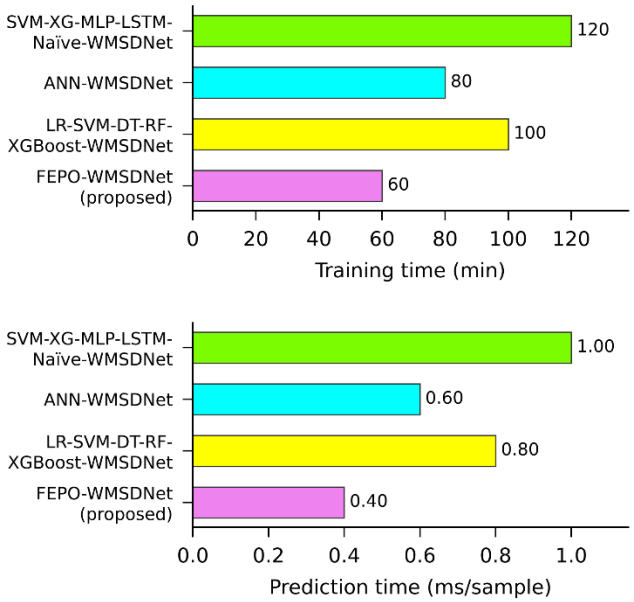


Fig. 20. Training and prediction-time comparison

Figure 20 compares computational time. Relative to SVM-XG-MLP-LSTM-Naïve-WMSDNet, ANN-WMSDNet, and LR-SVM-DT-RF-XGBoost-WMSDNet, FEPO-WMSDNet reported training-time reductions of 50%, 25%, and 40% and prediction-time reductions of 60%, 33.33%, and 50%, respectively. These measurements support future feasibility studies but do not constitute evidence of a deployed real-time workplace system.

4.4 Discussion

The performance analysis evaluates the integrated FEPO-WMSDNet framework on the UI-PRMD benchmark. Across the three selected shoulder-angle components, the proposed method reported lower MAPE, RMSE, and MAE and higher R^2 than the three WMSD-specific baseline methods evaluated in this study. It also reported higher MCC, accuracy, F1-score, precision, recall, and specificity, together with lower training and prediction times. These comparisons are limited to the evaluated baselines and should not be interpreted as evidence of general state-of-the-art superiority. The source dataset contains only 10 healthy subjects and consists of physical-rehabilitation movements rather than industrial work tasks. Although 10-fold LOSO evaluation prevents the same subject from appearing in training and testing within a fold, the small number of independent subjects, the use of derived rather than clinically adjudicated WMSD-risk labels, and the absence of an occupational cohort limit

external validity. The reported findings should therefore be interpreted as benchmark evidence for the computational framework, not as proof of effectiveness among textile workers. Future work should evaluate the model prospectively on larger, diverse, multi-site occupational cohorts with independent ergonomic annotation and should include component-wise ablation and stronger contemporary forecasting baselines. Figures 21 and 22 summarize the forecasting and classification comparisons, respectively.

Table 6. Overall AoT shoulder-angle forecasting performance

Shoulder angle component	Model	MAPE (%)	RMSE (°)	MAE (°)	R^2
Shoulder Abduction–Adduction	SVM-XG-MLP-LSTM-Naïve-WMSDNet [23]	18.5	0.36	0.28	0.650
	ANN-WMSDNet [24]	9.3	0.17	0.12	0.890
	LR-SVM-DT-RF-XGBoost-WMSDNet [25]	13.1	0.26	0.18	0.780
	FEPO-WMSDNet (Proposed)	3.5	0.06	0.04	0.985
Shoulder Internal–External Rotation	SVM-XG-MLP-LSTM-Naïve-WMSDNet [23]	20.1	0.39	0.30	0.620
	ANN-WMSDNet [24]	10.5	0.19	0.14	0.865
	LR-SVM-DT-RF-XGBoost-WMSDNet [25]	14.8	0.28	0.20	0.745
	FEPO-WMSDNet (Proposed)	4.2	0.08	0.06	0.965
Shoulder Flexion–Extension	SVM-XG-MLP-LSTM-Naïve-WMSDNet [23]	17.2	0.33	0.25	0.670
	ANN-WMSDNet [24]	8.9	0.16	0.11	0.895
	LR-SVM-DT-RF-XGBoost-WMSDNet [25]	12.5	0.24	0.16	0.795
	FEPO-WMSDNet (Proposed)	3.1	0.05	0.03	0.992

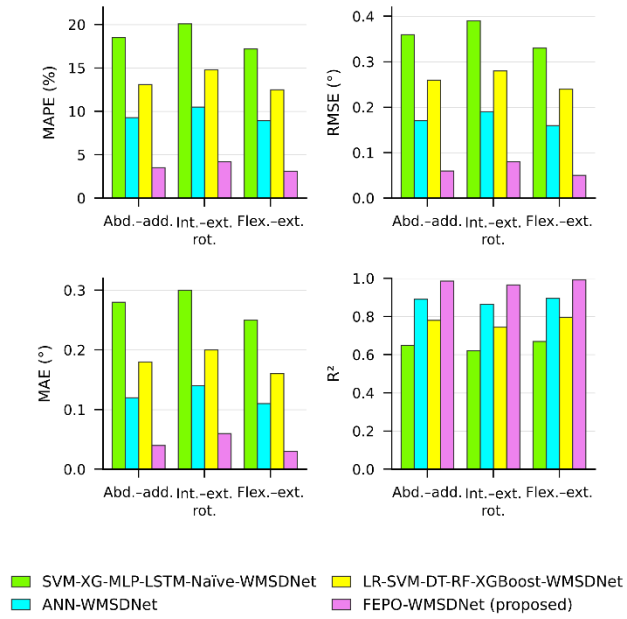


Fig. 21. Forecasting performance across shoulder-angle components (Abd.–add., abduction–adduction; Int.–ext. rot., internal–external rotation; Flex.–ext., flexion–extension)

Table 7. Overall WMSD-risk classification performance (each metric averaged separately)

Shoulder angle component	Model	Mean value (proportion)					
		MCC	Accuracy	F1-score	Precision	Recall	Specificity
Shoulder Abduction–Adduction	SVM-XG-MLP-LSTM-Naïve-WMSDNet [23]	0.6837	0.7630	0.7473	0.7342	0.7667	0.8106
	ANN-WMSDNet [24]	0.8643	0.9144	0.8903	0.8870	0.8996	0.9338
	LR-SVM-DT-RF-XGBoost-WMSDNet [25]	0.7935	0.8270	0.8105	0.8140	0.8173	0.8731
	FEPO-WMSDNet (Proposed)	0.9444	0.9703	0.9620	0.9620	0.9628	0.9842
Shoulder Internal–External Rotation	SVM-XG-MLP-LSTM-Naïve-WMSDNet [23]	0.7099	0.7334	0.7425	0.7020	0.8011	0.8118
	ANN-WMSDNet [24]	0.8906	0.8989	0.8899	0.8619	0.9137	0.9351
	LR-SVM-DT-RF-XGBoost-WMSDNet [25]	0.7931	0.8306	0.8135	0.7942	0.8363	0.8804
	FEPO-WMSDNet (Proposed)	0.9599	0.9512	0.9575	0.9322	0.9754	0.9881
Shoulder Flexion–Extension	SVM-XG-MLP-LSTM-Naïve-WMSDNet [23]	0.7294	0.7551	0.7525	0.7160	0.7995	0.7926
	ANN-WMSDNet [24]	0.8744	0.9139	0.8875	0.8770	0.9006	0.9301
	LR-SVM-DT-RF-XGBoost-WMSDNet [25]	0.7946	0.8365	0.8099	0.8035	0.8078	0.8643
	FEPO-WMSDNet (Proposed)	0.9567	0.9732	0.9644	0.9622	0.9674	0.9742

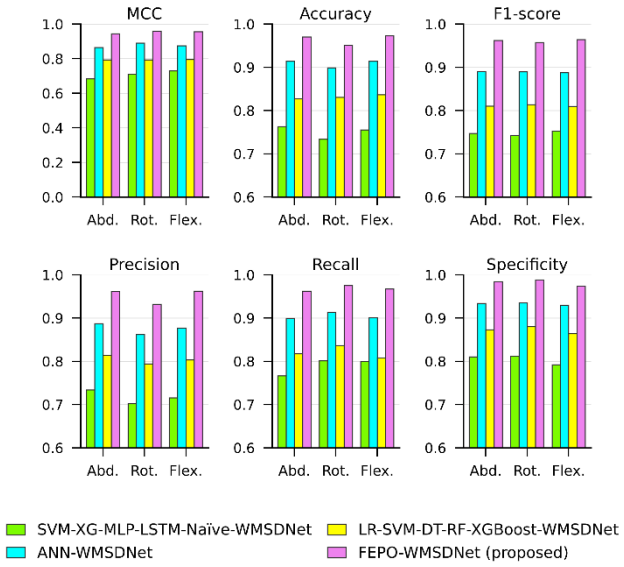


Fig. 22. Classification performance across shoulder-angle components (Abd., abduction–adduction; Rot., internal–external rotation; Flex., flexion–extension)

For an additional controlled comparison, CNN, LSTM, and BiLSTM baselines were implemented using the same UI-PRMD subject-level partitions and preprocessing protocol. **Table 8** reports their performance across five matched runs together with two-sided paired t-test p-values relative to FEPO-WMSDNet. These tests assess the observed differences within the evaluated protocol and do not establish superiority over model families that were not experimentally evaluated.

Table 8. Experimental comparison across five matched runs with paired t-tests

Method	Accuracy (%), mean ± SD	Precision (%)	Recall (%)	F1-score (%)	Paired t-test p-value
CNN	92.84 ± 0.72	92.15	92.48	92.31	< 0.01
LSTM	93.91 ± 0.65	93.56	93.74	93.65	< 0.01
BiLSTM	95.07 ± 0.51	94.81	94.96	94.88	0.006
Proposed FEPO-WMSDNet	96.48 ± 0.14	95.26 ± 0.11	96.90 ± 0.13	96.07 ± 0.12	–

Table 9 reports two-sided 95% confidence intervals for FEPO-WMSDNet across the five independent runs. The intervals were calculated from the run-level means using the t distribution with four degrees of freedom.

Table 9. Mean performance and 95% confidence intervals across five runs

Metrics	Mean	95% confidence interval
Accuracy (%)	96.48	[96.31, 96.66]
Precision (%)	95.26	[95.13, 95.39]
Recall (%)	96.90	[96.73, 97.07]
F1-score (%)	96.07	[95.92, 96.22]
MCC	0.954	[0.952, 0.957]

Table 10 lists the five run-level results and their mean ± sample standard deviation. The small dispersion indicates stable optimization across these runs, although run-level stability is distinct from external generalization to new occupational populations.

Table 10. Stability analysis across five independent runs

Run	Accuracy (%)	Precision (%)	Recall (%)	F1-score (%)	MCC
Run 1	96.32	95.14	96.71	95.91	0.952
Run 2	96.58	95.31	96.95	96.12	0.955
Run 3	96.47	95.20	96.86	96.03	0.954
Run 4	96.66	95.42	97.08	96.24	0.957
Run 5	96.39	95.23	96.89	96.06	0.953
Mean ± SD	96.48 ± 0.14	95.26 ± 0.11	96.90 ± 0.13	96.07 ± 0.12	0.954 ± 0.002

Table 11 reports exploratory two-sided Wilcoxon signed-rank comparisons with the three WMSD-specific baseline methods across matched LOSO subject folds. The reported p-values are unadjusted; all are below 0.05, but they should be interpreted together with effect sizes, the small subject cohort, and the absence of an external test dataset.

Table 11. Exploratory Wilcoxon signed-rank comparisons

across matched LOSO folds

Method	Mean accuracy (%)	Statistical test	Unadjusted p-value	Significance
SVM-XG-MLP-LSTM-Naïve-WMSDNet	84.70	Wilcoxon signed-rank	<0.001	Significant
ANN-WMSDNet	91.60	Wilcoxon signed-rank	0.003	Significant
LR-SVM-DT-RF-XGBoost-WMSDNet	93.20	Wilcoxon signed-rank	0.012	Significant
Proposed FEPO-WMSDNet	96.48	–	–	–

5 Conclusion

This study developed FEPO-WMSDNet for AoT forecasting of shoulder kinematics and classification of ergonomics-rule-derived risk windows. The framework integrates FEINN, the Puma Optimizer, and CK-FANN and was evaluated through secondary analysis of the publicly available UI-PRMD Vicon joint-angle data from 10 healthy subjects. The proposed method reported improved forecasting, classification, and computational-time measures relative to the three WMSD-specific baselines evaluated here. However, UI-PRMD is a physical-rehabilitation dataset, not an industrial WMSD cohort; its participants were not textile workers, and its original records do not contain WMSD diagnoses or RULA/ISO risk labels. The present results therefore demonstrate benchmark performance of the integrated framework but do not establish workplace effectiveness, general state-of-the-art superiority, or the independent necessity of each component. Future work should validate the model on prospectively collected occupational data, include expert ergonomic ground truth, expand the participant population, compare contemporary forecasting architectures experimentally, and conduct a systematic component-wise ablation study before real-time workplace deployment is considered.

Conflict of Interest: The author declares no competing interests.

Data Availability Statement: This study used the publicly available UI-PRMD (University of Idaho Physical Rehabilitation Movements Dataset) introduced by Vakanski et al. [39]. The dataset is available at http://webpages.uidaho.edu/ui-prmd/, and the data descriptor is available at https://doi.org/10.3390/data3010002. No new human-subject data were collected for the present study.

Ethical Statement: The present study was a secondary analysis of the publicly available UI-PRMD dataset collected by Vakanski et al. [39]. As reported in the original data descriptor, the source study obtained written informed consent from all participants under a board-approved protocol. No new participants were recruited and no new human-subject data were collected for the present analysis; therefore, additional institutional ethical approval was not required for this secondary study.

Funding Declaration: The author received no funding for this study.

REFERENCES

[1] Bao, N., Zheng, X., Fan, Y., Simeone, A. and Bao, R., 2025. *Enhancing garment manufacturing efficiency through human-centered scheduling.* Production Engineering, pp.1-14.

[2] Talapatra, S., Parvez, M.S., Saha, P. and Kibria, M.G., 2024. *Assessing the impact of critical risk factors on the development of musculoskeletal disorders: a structural equation modelling approach.* Theoretical Issues in Ergonomics Science, 25(3), pp.343-368.

[3] Monteiro, V.A., Marzoque, H.J., Batista, M.L., Alencar, M.D.C.B.D., Pereira, L.D. and Nääs, I.D.A., 2025. *Navigating Occupational Hazards: Musculoskeletal Disorders Among Slaughterhouse Workers in Brazil.* Safety, 11(2), p.39.

[4] Fouad, A.M., Fahim, A.E., Bedewy, A.A., Al-Touny, A. and Al-Touny, S.A., 2024. *Work-related musculoskeletal complaints and ergonomic risk factors among Egyptian anesthesiologists: a cross-sectional study.* BMC Public Health, 24(1), p.279.

[5] Jin, X., Dong, Y., Yang, L., Huang, W., Cao, L., Zhang, Z. and He, L., 2025. *Ergonomic interventions to improve musculoskeletal disorders among vehicle assembly workers: a one-year longitudinal study.* BMC Public Health, 25(1), p.824.

[6] Aghamohammadi, A., Beheshti Shirazi, S.A., Banihashem, S.Y., Shishechi, S., Ranjbarzadeh, R., Jafarzadeh Ghoushchi, S. and Bendechache, M., 2024. *A deep learning model for ergonomics risk assessment and sports and health monitoring in self-occluded images.* Signal, Image and Video Processing, 18(2), pp.1161-1173.

[7] Xiaochun, C., 2025. *Research on entertainment robots based on artificial intelligence interaction for human posture recognition and sports activity monitoring.* Entertainment Computing, 52, p.100761.

[8] Dasgupta, A., Sharma, R., Mishra, C. and Nagaraja, V.H., 2023. *Machine learning for optical motion capture-driven musculoskeletal modelling from inertial motion capture data.* Bioengineering, 10(5), p.510.

[9] Ansari, S., Du, H., Naghdy, F. and Stirling, D., 2022. *Automatic driver cognitive fatigue detection based on upper body posture variations.* Expert Systems with Applications, 203, p.117568.

[10] Lee, Y.C. and Lee, C.H., 2022. *SEE: a proactive strategy-centric and deep learning-based ergonomic risk assessment system for risky posture recognition.* Advanced Engineering Informatics, 53, p.101717.

[11] Raza, M., Bhushan, R.K., Khan, A.A., Ali, A.M., Khamaj, A. and Alam, M.M., 2024, December. *Prevalence of*

Musculoskeletal Disorders in Heavy Vehicle Drivers and Office Workers: A Comparative Analysis Using a Machine Learning Approach. In Healthcare (Vol. 12, No. 24, p. 2560). MDPI.

[12] Beniwal, M., Singh, A. and Kumar, N., 2023. *Forecasting long-term stock prices of global indices: A forward-validating Genetic Algorithm optimization approach for Support Vector Regression.* Applied Soft Computing, 145, p.110566.

[13] Tlili, F., Haddad, R., Bouallegue, R. and Mezghani, N., 2021. *A real-time posture monitoring system towards bad posture detection.* Wireless Personal Communications, 120(2), pp.1207-1227.

[14] Jaiswal, A., Kumar, M. and Meisingset, I., 2025. S*upportPrim CDSS: A Clinical Decision Support System Architecture Based on Microservices for Non-Specific Musculoskeletal Disorders.* International Journal of Medical Informatics, p.105919.

[15] Seixas-Lopes, F.A., Lopes, C., Marques, M., Agostinho, C. and Jardim-Goncalves, R., 2024. *Musculoskeletal disorder (MSD) health data collection, personalized management and exchange using fast healthcare interoperability resources (FHIR).* Sensors, 24(16), p.5175.

[16] Antwi-Afari, M.F., Qarout, Y., Herzallah, R., Anwer, S., Umer, W., Zhang, Y. and Manu, P., 2022. *Deep learning-based networks for automated recognition and classification of awkward working postures in construction using wearable insole sensor data.* Automation in construction, 136, p.104181.

[17] Jiao, Z., Huang, K., Wang, Q., Jia, G., Zhong, Z. and Cai, Y., 2024. *Improved REBA: deep learning based rapid entire body risk assessment for prevention of musculoskeletal disorders.* Ergonomics, 67(10), pp.1356-1370.

[18] Ciccarelli, M., Corradini, F., Germani, M., Menchi, G., Mostarda, L., Papetti, A. and Piangerelli, M., 2023. *SPECTRE: a deep learning network for posture recognition in manufacturing.* Journal of Intelligent Manufacturing, 34(8), pp.3469-3481.

[19] Sheik Abdullah, A., Parkavi, R. and Geetha, S., 2025. *A diagnostic model for evaluating the posture recognition using multivariate Gaussian deep CNN for determining musculoskeletal disorders.* Multimedia Tools and Applications, pp.1-39.

[20] Huang, K., Jia, G., Wang, Q., Cai, Y., Zhong, Z. and Jiao, Z., 2024. *Spatial relationship-aware rapid entire body fuzzy assessment method for prevention of work-related musculoskeletal disorders.* Applied Ergonomics, 115, p.104176.

[21] Ogundokun, R.O., Maskeliūnas, R., Misra, S. and Damasevicius, R., 2022. Hyb*rid inceptionv3-svm-based approach for human posture detection in health monitoring systems.* Algorithms, 15(11), p.410.

[22] Su, J.M., Chang, J.H., Indrayani, N.L.D. and Wang, C.J., 2023. *Machine learning approach to determine the decision rules in ergonomic assessment of working posture in sewing machine operators.* Journal of Safety Research, 87, pp.15-26.

[23] Matos, L.M., Dias, P., Matta, A., Machado, D., Sampaio, R., Pilastri, A. and Cortez, P., 2024. *Proactive prevention of work-related musculoskeletal disorders using a motion capture system and time series machine learning.* Engineering Applications of Artificial Intelligence, 138, p.109353.

[24] Yildiz, E. and Das, M., 2025. *Design and experimental verification of a posture correction system: Development of an artificial neural network to predict the effectiveness of the developed system to correct poor posture.* International Journal of Human–Computer Interaction, 41(15), pp.9848-9858.

[25] Jung, S., Kim, B., Kim, Y.J., Lee, E.S., Kang, D. and Kim, Y., 2025. *Prediction of Work-relatedness of Shoulder Musculoskeletal Disorders as by Using Machine Learning.* Safety and Health at Work, 16(1), pp.113-121.

[26] Zhang, N., Xu, K., Yin, Z.Y. and Li, K.Q., 2025. *Transfer learning-enhanced finite element-integrated neural networks.* International Journal of Mechanical Sciences, 290, p.110075.

[27] Abdollahzadeh, B., Khodadadi, N., Barshandeh, S., Trojovský, P., Gharehchopogh, F.S., El-kenawy, E.S.M., Abualigah, L. and Mirjalili, S., 2024. *Puma optimizer (PO): a novel metaheuristic optimization algorithm and its application in machine learning.* Cluster Computing, 27(4), pp.5235-5283.

[28] Karakurt, M., Saygılı, H. and Karcı, A., 2025. *Karcı fractional artificial neural networks (KarcıFANN): a new artificial neural networks model without learning rate and its problems.* Turkish Journal of Electrical Engineering and Computer Sciences, 33(3), pp.248-263.

[29] Lim, B., Arık, S.Ö., Loeff, N. and Pfister, T., 2021. *Temporal fusion transformers for interpretable multi-horizon time series forecasting.* International journal of forecasting, 37(4), pp.1748-1764.

[30] Zhou, H., Zhang, S., Peng, J., Zhang, S., Li, J., Xiong, H. and Zhang, W., 2021, May. *Informer: Beyond efficient transformer for long sequence time-series forecasting.* In Proceedings of the AAAI conference on artificial intelligence (Vol. 35, No. 12, pp. 11106-11115).

[31] Wu, H., Xu, J., Wang, J. and Long, M., 2021. *Autoformer: Decomposition transformers with auto-correlation for long-term series forecasting.* Advances in neural information processing systems, 34, pp.22419-22430.

[32] Nie, Y., Nguyen, N.H., Sinthong, P. and Kalagnanam, J., 2022. *A time series is worth 64 words: Long-term forecasting with transformers.* arXiv preprint arXiv:2211.14730.

[33] Bai, S., Kolter, J.Z. and Koltun, V., 2018. *An empirical evaluation of generic convolutional and recurrent networks for sequence modeling.* arXiv preprint arXiv:1803.01271.

[34] Raissi, M., Perdikaris, P. and Karniadakis, G.E., 2019. *Physics-informed neural networks: A deep learning framework for solving forward and inverse problems involving nonlinear partial differential equations.* Journal of Computational physics, 378, pp.686-707.

[35] Mao, W., Liu, M., Salzmann, M. and Li, H., 2019. *Learning trajectory dependencies for human motion*

prediction. In Proceedings of the IEEE/CVF international conference on computer vision (pp. 9489-9497).

[36] Raissi, M., Perdikaris, P., Ahmadi, N. and Karniadakis, G.E., 2024. *Physics-informed neural networks and extensions.* arXiv preprint arXiv:2408.16806.

[37] Farea, A., Yli-Harja, O. and Emmert-Streib, F., 2024. *Understanding physics-informed neural networks: Techniques, applications, trends, and challenges.* Ai, 5(3), pp.1534-1557.

[38] Zachariah, N. and Charitha, K., 2026. *Novel Graph Autoencoder Hybrid for Dimensionality Reduction in Ergonomic Risk Classification: Modeling Posture as Skeletal Graphs.* Journal of Human-Centered Design for Manufacturing, 2(1), pp.45-64.

[39] Vakanski, A., Jun, H.-P., Paul, D. and Baker, R., 2018. *A data set of human body movements for physical rehabilitation exercises.* Data, 3(1), p.2. https://doi.org/10.3390/data3010002.